

**A quantum-chemical perspective on the  
laser-induced alignment and orientation dynamics  
of the CH<sub>3</sub>X (X = F, Cl, Br, I) molecules**

Irén Simkó,<sup>\*</sup> Attila G. Császár, and Tamás Szidarovszky<sup>†</sup>

*Institute of Chemistry, ELTE Eötvös Loránd University and  
ELKH-ELTE Complex Chemical Systems Research Group,  
H-1117 Budapest, Pázmány Péter sétány 1/A, Hungary*

Kalyani Chordiya<sup>\*</sup> and Mousumi Upadhyay Kahaly<sup>‡</sup>

*ELI-ALPS, ELI-HU Non-Profit Ltd., Dugonics tér 13 and  
University of Szeged, Dóm tér 9, H-6720 Szeged, Hungary*

(Dated: February 1, 2022)

## Abstract

Motivated by recent experiments, the laser-induced alignment-and-orientation (A&O) dynamics of the prolate symmetric top  $\text{CH}_3\text{X}$  ( $\text{X} = \text{F}, \text{Cl}, \text{Br}, \text{I}$ ) molecules is investigated, with particular emphasis on the effect of halogen substitution on the rotational constants, dipole moments, and polarizabilities of these species, as these quantities determine the A&O dynamics. Insight into possible control schemes for preferred A&O dynamics of halogenated molecules and best practices for A&O simulations are provided, as well. It is shown that for accurate A&O-dynamics simulations it is necessary to employ large basis sets and high levels of electron correlation when computing the rotational constants, dipole moments, and polarizabilities. The benchmark-quality values of these molecular parameters, corresponding to the equilibrium, as well as the vibrationally averaged structures are obtained with the help of the focal-point analysis (FPA) technique and explicit electronic-structure computations utilizing the gold-standard CCSD(T) approach, basis sets up to quintuple-zeta quality, core-correlation contributions and, in particular, relativistic effects for  $\text{CH}_3\text{Br}$  and  $\text{CH}_3\text{I}$ . It is shown that the different A&O behavior of the  $\text{CH}_3\text{X}$  molecules in the optical regime is mostly caused by the differences in their polarizability anisotropy, in other terms, the size of the halogen atom. In contrast, the A&O dynamics of the  $\text{CH}_3\text{X}$  series induced by an intense few-cycle THz pulse is mostly governed by changes in the rotational constants, due to the similar dipole moments of the  $\text{CH}_3\text{X}$  molecules. The A&O dynamics is most sensitive to the  $B$  rotational constant: even the difference between its equilibrium and vibrationally-averaged values results in noticeably different A&O dynamics. The contribution of rotational states having different symmetry, weighted by nuclear-spin statistics, to the A&O dynamics is also studied.

---

\* Equal contribution.

† [tamas.janos.szidarovszky@ttk.elte.hu](mailto:tamas.janos.szidarovszky@ttk.elte.hu)

‡ [mousumi.upadhyaykahaly@eli-alps.hu](mailto:mousumi.upadhyaykahaly@eli-alps.hu)

## CONTENTS

I. Introduction	4
II. Theory	5
III. Computational details	10
IV. On molecular parameters important for A&O dynamics	12
A. Effects of electron correlation and basis set size on molecular parameters	12
B. Substituent effects on chemical properties	15
V. Single-optical-pulse alignment	18
A. The role of different molecular parameters	19
1. The role of polarizability anisotropy	21
2. The role of rotational constants	22
3. Sensitivity to the accuracy of molecular parameters	23
4. The role of symmetry and nuclear spin statistical weights	23
B. The role of experimental parameters	25
1. Pulse energy	25
2. Temperature	26
VI. Single-THz-pulse alignment and orientation	26
A. The role of pulse parameters, adiabatic and non-adiabatic regimes	27
B. The role of molecular parameters	29
1. Rotational constants, dipole moment, and polarizability	29
2. Sensitivity to the accuracy of molecular parameters	32
3. The role of symmetry and nuclear-spin-statistical weights	33
VII. Summary and conclusions	34
VIII. Acknowledgements	36
IX. Data availability	37
X. Conflict of interest	37
References	37

## I. INTRODUCTION

Laser-induced molecular rotational alignment and orientation (A&O) has been investigated, both theoretically and experimentally, for a number of decades. Different A&O realizations have been proposed and demonstrated [1–4], such as adiabatic [5–8] and non-adiabatic A&O [9–13], A&O along one [11, 14, 15], two [6], or three dimensions [16–19], using linearly [10, 11, 14] or circularly [15] polarized pulses, employing single [14, 15] or multiple pulses [9, 10, 16, 18], utilizing optical [10, 14, 16] and/or terahertz (THz) [10, 20, 21] pulses, optical centrifuges [6], alignment in helium droplets [14, 15], to name just a few developments. In addition to the various practical applications of A&O in molecular sciences, including, but not limited to rotational coherence spectroscopy (which can be used to determine accurate rotational constants [22–25]), chemical reaction control, isotope and photofragment separation, and molecule trapping, the appearance of attochemistry [26–28] has stimulated renewed interest in A&O dynamics. Since molecular rotations typically proceed on a picosecond to nanosecond timescale, efficient rotational A&O allows for carrying out femtosecond or attosecond dynamics experiments in a molecule-fixed frame, providing potentially much richer information than experiments carried out on isotropic samples [29–31]. Furthermore, coherent molecular rotations can be exploited to provide unique media for high-harmonics generation [32–34].

The photochemistry of various methyl halide molecules, that is  $\text{CH}_3\text{F}$ ,  $\text{CH}_3\text{Cl}$ ,  $\text{CH}_3\text{Br}$ , and  $\text{CH}_3\text{I}$ , has drawn attention due partially to the molecules’ impact on atmospheric science. These halogen-containing molecules have a simple structure (they are symmetric tops) and their interaction with laser fields has often been studied *via* different experimental and theoretical methods. For example, Hamilton *et al.* [35] studied, both experimentally and theoretically, nonadiabatic alignment of  $\text{CH}_3\text{I}$ , focusing on the shape and intensity of the alignment revivals, including their dependence on the pulse duration and their behavior at long times, where centrifugal distortion effects become important. Recent experiments have been performed by Luo *et al.* [36] to investigate the A&O dynamics of thermally averaged and quantum-state-selected  $\text{CH}_3\text{I}$  molecules, employing intense femtosecond 800 nm laser fields. The same group investigated how the laser-induced alignment affects the double ionization and chemical bond rearrangement in  $\text{CH}_3\text{Cl}$  [37]. In another study, He *et al.* [38] measured the effect of laser-induced alignment on the ion yields of quantum-state-selected

CH<sub>3</sub>I and CH<sub>3</sub>Br molecules, in the 10–1000 TW cm<sup>−2</sup> intensity regime for the ionization laser. The angle-dependent strong-field ionization of halomethanes was studied by Sándor *et al.* [39], who employed short and intense optical laser pulses to align the molecules and revealed that even though their electronic structure has similar character, CH<sub>3</sub>F, CH<sub>3</sub>Cl, and CH<sub>3</sub>Br ionize *via* different mechanisms.

Recently, in order to aid experimentalists carrying out such simulations, a user-friendly and cross-platform software was developed, called LIMA O [40], where the acronym stands for “laser-induced molecular alignment and orientation”. Although running A&O dynamics simulations with LIMA O is not difficult, the program does require, as all A&O simulations, molecular parameters that might not be readily available in the literature. In such cases the most straightforward approach is to compute these parameters using standard quantum-chemical (more precisely, electronic-structure) techniques [41]. The main motivation of this work was to identify the quantum-chemical techniques suitable for obtaining accurate A&O-related molecular parameters, and to study how halogen substitution affects A&O dynamics through these parameters. We also investigate, in a practical sense, some general features of running A&O simulations.

## II. THEORY

During this study, the laser-induced rotational dynamics was simulated by directly solving the appropriate time-dependent Schrödinger equation (TDSE), as implemented in the code LIMA O [40]. In short, LIMA O utilizes a field-free eigenstate basis to solve the TDSE

$$i\hbar\partial_t|\Psi(t)\rangle = \hat{H}(t)|\Psi(t)\rangle, \quad (1)$$

based on the time-dependent Hamiltonian  $\hat{H}(t)$  of a molecule interacting with an external electric field. By treating electronic excitation perturbatively,  $\hat{H}(t)$  can be written [42] as

$$\hat{H}(t) = \hat{H}_0 - \boldsymbol{\varepsilon}(t)\hat{\boldsymbol{\mu}} - \frac{1}{2}\boldsymbol{\varepsilon}(t)(\hat{\boldsymbol{\alpha}}\boldsymbol{\varepsilon}(t)), \quad (2)$$

where  $\hat{H}_0$  is the field-free rotational Hamiltonian,  $\hat{\boldsymbol{\mu}}$  and  $\hat{\boldsymbol{\alpha}}$  are the permanent molecular dipole and polarizability operators, respectively, and  $\boldsymbol{\varepsilon}(t)$  is the three-dimensional (3D) external electric-field vector. Assuming a linearly polarized external field, *i.e.*,  $\boldsymbol{\varepsilon}(t) = (0, 0, \varepsilon(t))$ ,

and using the  $|\Psi^{JMn}\rangle$  field-free eigenstates, satisfying the time-independent Schrödinger equation

$$\hat{H}_0|\Psi^{JMn}\rangle = E^{Jn}|\Psi^{JMn}\rangle, \quad (3)$$

one can construct the matrix representation of Eq. (2), yielding the matrix elements

$$\begin{aligned} & \langle \Psi^{JMn} | \hat{H}(t) | \Psi^{J'M'n'} \rangle = \\ & E^{Jn} \delta_{JJ'} \delta_{nn'} \delta_{MM'} - \langle \Psi^{JMn} | \boldsymbol{\varepsilon}(t) \boldsymbol{\mu} | \Psi^{J'M'n'} \rangle - \frac{1}{2} \langle \Psi^{JMn} | \boldsymbol{\varepsilon}(t) (\boldsymbol{\alpha} \boldsymbol{\varepsilon}(t)) | \Psi^{J'M'n'} \rangle = \\ & E^{Jn} \delta_{JJ'} \delta_{nn'} \delta_{MM'} - \\ & \varepsilon(t) \sum_{k=-1}^1 \langle \Psi^{JMn} | D_{0k}^1 * \mu^{\text{BF},(1,k)} | \Psi^{J'M'n'} \rangle - \\ & \frac{\varepsilon^2(t)}{\sqrt{6}} \left[ \sum_{k=-2}^2 \langle \Psi^{JMn} | D_{0k}^2 * \alpha^{\text{BF},(2,k)} | \Psi^{J'M'n'} \rangle - \frac{1}{\sqrt{2}} \langle \Psi^{JMn} | \alpha^{\text{BF},(0)} | \Psi^{J'M'n'} \rangle \right]. \end{aligned} \quad (4)$$

In Eqs. (3) and (4),  $J$  is the rotational angular-momentum quantum number, quantum number  $M$  refers to the projection of the angular momentum onto the space-fixed  $z$  axis,  $n$  represents all the other quantum numbers, and  $E^{Jn}$  are field-free molecular eigenenergies. In the same equations,  $\mu^{\text{BF},(1,k)}$  and the  $\alpha^{\text{BF},(2,k)}$  and  $\alpha^{\text{BF},(0)}$  pair are the body-fixed molecular dipole and polarizability in the spherical-basis representation [43, 44], respectively, for which transformation to the space-fixed components can be carried out *via* the Wigner-D matrices  $D_{0k}^i$  [43, 44]. The specific form of  $|\Psi^{JMn}\rangle$  and the matrix elements of Eq. (4) depend on the type of molecule (rotational top) considered; for details, see Ref. 40. In this work only symmetric tops are investigated; therefore,  $|\Psi^{JMn}\rangle$  are the symmetric top eigenfunctions  $|JKM\rangle$ , where  $K$  is the quantum number corresponding to the projection of the angular momentum onto the body-fixed  $z$  axis. For a given initial wave function,  $|\Psi^{JMn}\rangle$ , and a specific external electric field,  $\boldsymbol{\varepsilon}(t)$ , the TDSE is solved by numerical propagation, employing the Hamiltonian matrix elements given in Eq. (4).

LIMAO allows simulations at finite rotational temperatures under the assumption that the initial population in the different rotational eigenstates satisfies the Boltzmann distribution. The population of the  $i$ th eigenstate,  $P_i$ , at thermal equilibrium is then given by

$$P_i = \frac{g_i e^{-\frac{E_i}{k_B T}}}{Q_{\text{rot}}(T)}, \quad (5)$$

where  $Q_{\text{rot}}(T) = \sum_l g_l e^{-\frac{E_l}{kT}}$  is the rotational partition function,  $k_B$  is Boltzmann's constant,  $E_i$  is the eigenenergy of the  $i$ th rotational state, and  $g_i$  stands for the nuclear spin statistical weight (NSSW) of the  $i$ th rotational eigenstate [44]. The occurrence of NSSWs in Eq. (5) is a direct consequence of the Pauli exclusion principle [44]. In brief, rotational eigenstates can only be paired with nuclear spin functions for which the product rotational-nuclear spin wave function has proper nuclear permutation symmetry, *i.e.*, it changes sign (remains unchanged) to the permutation of identical fermionic (bosonic) nuclei. NSSW plays an important role in the relative populations of different rotational states at finite temperatures. The NSSWs of rotational states can be determined following the procedure described in the supplementary material of Ref. 40.

The temporal evolution of the expectation value of a physical quantity  $\hat{A}$ ,  $\langle \hat{A} \rangle(t)$ , is then expressed as

$$\langle \hat{A} \rangle(t) = \frac{1}{Q_{\text{rot}}(T)} \sum_i \langle \Psi^{(i)}(t) | \hat{A} | \Psi^{(i)}(t) \rangle g_i e^{-\frac{E_i}{kT}}, \quad (6)$$

where  $\Psi^{(i)}(t)$  is the time-dependent rotational wave packet when the initial condition is set to be the  $i$ th rotational eigenstate;

$$\Psi^{(i)}(t) = \sum_{JMn} C_{JMn}^{(J_i M_i n_i)}(t) | \Psi^{JMn} \rangle, \quad (7)$$

where  $C_{JMn}^{(J_i M_i n_i)}(t)$  are the time-dependent expansion coefficients. Thus,

$$\langle \Psi^{(i)}(t) | \hat{A} | \Psi^{(i)}(t) \rangle = \sum_{JMn, J'M'n'} C_{JMn}^{(J_i M_i n_i)*}(t) C_{J'M'n'}^{(J_i M_i n_i)}(t) \langle \Psi^{JMn} | \hat{A} | \Psi^{J'M'n'} \rangle, \quad (8)$$

with  $C_{JMn}^{(J_i M_i n_i)}(t=0) = \delta_{JJ_i} \delta_{MM_i} \delta_{nn_i}$ . For quantifying the alignment,  $\hat{A} = \cos^2(\theta)$  can be used, while for the orientation it is appropriate to utilize  $\hat{A} = \cos(\theta)$ , where  $\theta$  is the angle between the laboratory-fixed and body-fixed  $z$  axes. The specific form of the  $\langle \Psi^{JMn} | \cos(\theta) | \Psi^{J'M'n'} \rangle$  and  $\langle \Psi^{JMn} | \cos^2(\theta) | \Psi^{J'M'n'} \rangle$  matrix elements depend on the type of molecule considered; see Ref. 40 for details. The matrix elements for  $\cos^2(\theta)$  and the  $|JKM\rangle$

symmetric-top eigenfunctions are

$$\langle JKM | \cos^2(\theta) | J'K'M' \rangle = \frac{1}{3}\delta_{JJ'}\delta_{KK'}\delta_{MM'} + \delta_{MM'}\frac{2}{3}\sqrt{(2J+1)(2J'+1)}(-1)^{M+K'} \begin{pmatrix} J & 2 & J' \\ M & 0 & -M \end{pmatrix} \begin{pmatrix} J & 2 & J' \\ K & 0 & -K' \end{pmatrix} \quad (9)$$

and

$$\langle JKM | \cos(\theta) | J'K'M' \rangle = \delta_{MM'}\sqrt{(2J+1)(2J'+1)}(-1)^{M+K'} \begin{pmatrix} J & 1 & J' \\ M & 0 & -M \end{pmatrix} \begin{pmatrix} J & 1 & J' \\ K & 0 & -K' \end{pmatrix}, \quad (10)$$

where  $\begin{pmatrix} \cdot & \cdot & \cdot \end{pmatrix}$  denotes the Wigner 3- $j$  symbols [43]. It follows from the properties of the Wigner 3- $j$  symbols that  $\langle JKM | \cos^2(\theta) | J'K'M' \rangle$  can be nonzero only if  $M = M'$ ,  $K = K'$ , and  $|J - J'| \leq 2$ . Similarly,  $\langle JKM | \cos(\theta) | J'K'M' \rangle$  can be nonzero only if  $M = M'$ ,  $K = K'$ , and  $|J - J'| \leq 1$ .

Depending on the temporal profile of the exciting pulse(s), one might achieve adiabatic or non-adiabatic, also called field-free, A&O [1]. Adiabatic A&O occurs when the external field changes much slower than the characteristic rotational timescale of the molecule, resulting in A&O only during the presence of the external field. On the other hand, non-adiabatic A&O can occur when the exciting pulse is shorter than the characteristic rotational timescale of the molecule, leading to the formation of a rotational wave packet, which might show, under field-free conditions, A&O after the external field subsides. In what follows we briefly describe how specific patterns appear in the temporal evolution of field-free A&O dynamics of molecules.

Let us start with a qualitative description [22]. Initially, in the absence of an external field, the molecules have isotropic distribution, the corresponding values of alignment and orientation are exactly 1/3 and 0, respectively. Then, assuming a polarized laser pulse, a rotational wave packet is formed and the molecules are aligned or oriented parallel to the polarization axis. This arrangement, however, quickly disappears due to the dispersion of the rotational wave packet and the sample shows a pseudoisotropic distribution. After a certain time rephasing occurs, causing a transient increase in the A&O, called the “revival”. This is followed again by dispersion and the cycle starts over.

Now, let us turn to a more formal description [22]. The laser pulse excites the sample



and creates a rotational wave packet, see Eq. (7). If the external field is turned off at  $t_{\text{end}}$ , the time-dependent coefficients have the form

$$C_{JMn}^{(J_i M_i n_i)}(t + t_{\text{end}}) = \exp\left(-\frac{i}{\hbar} E^{Jn} t\right) C_{JMn}^{(J_i M_i n_i)}(t_{\text{end}}), \quad (11)$$

corresponding to the field-free time evolution after  $t_{\text{end}}$ . Then, the expectation value of  $\hat{A}$  after the pulse is

$$\langle \hat{A} \rangle(t + t_{\text{end}}) = \sum_{JMn, J'M'n'} C_{JMn}^{(J_i M_i n_i)*}(t_{\text{end}}) C_{J'M'n'}^{(J_i M_i n_i)}(t_{\text{end}}) \langle \Psi^{JMn} | \hat{A} | \Psi^{J'M'n'} \rangle \exp\left(-\frac{i}{\hbar} \omega_{J'n', Jn} t\right), \quad (12)$$

where  $\omega_{J'n', Jn} = E^{J'n'} - E^{Jn}$ . The time dependence of  $\langle \hat{A} \rangle(t + t_{\text{end}})$  is a result of the superposition of the exponential terms with different  $\omega_{J'n', Jn}$  frequencies. One could expect that the superposition never results in constructive interference, but this is not the case. In the case of the rotational wave packet of linear or symmetric tops, the  $\omega_{J'n', Jn}$  frequencies have the form

$$\omega_{J'n', Jn} = k_{J'n', Jn} \Omega \quad \text{or} \quad \omega_{J'n', Jn} = k_{J'n', Jn} \Omega + \Phi, \quad (13)$$

where  $k_{J'n', Jn}$  is an integer, while  $\Omega$  and  $\Phi$  are constants. Therefore, a constructive interference occurs in  $\langle \hat{A} \rangle(t + t_{\text{end}})$  if  $t$  is an integer multiple of  $h/\Omega$ , where  $h$  is Planck's constant, leading to an observable "revival" [22].

Next, we describe how revivals of symmetric-top molecules are manifested in the orientation and alignment. The matrix element of the orientation can be nonzero only if  $K = K'$  and  $|J - J'| \leq 1$  (see Eq. (10)), so only these terms contribute to the superposition. Therefore, using the  $E^{J,K} = hcBJ(J+1) + hc(A-B)K^2$  energy formula of prolate symmetric tops,

$$\omega_{J'K', JK} = E^{J'K'} - E^{JK} = \begin{cases} 2hcBJ + 2hcB, & \text{if } J' = J + 1 \text{ and } K' = K \\ 0, & \text{if } J' = J \text{ and } K' = K, \end{cases} \quad (14)$$

so the  $J' = J$  contributions are constant in time and the time periodicity of the orientation revivals is  $T_{\text{rev}} = 1/(2Bc)$  due to the  $J' = J + 1$  contributions. In the case of alignment, the

matrix element can be nonzero only if  $K = K'$  and  $|J - J'| \leq 2$  (see Eq. (9)). Thus,

$$\omega_{J'K',JK} = E^{J'K'} - E^{JK} = \begin{cases} 4hcBJ + 6hcB, & \text{if } J' = J + 2 \text{ and } K' = K \\ 2hcBJ + 2hcB, & \text{if } J' = J + 1 \text{ and } K' = K \\ 0, & \text{if } J' = J \text{ and } K' = K. \end{cases} \quad (15)$$

In practice, the contributions from the different  $J' = J + 1$  cases cancel out. Then, only the  $J' = J + 2$  terms contribute to the time evolution of the alignment, resulting in revivals with alternating polarity (half revival) and with  $T_{\text{rev}} = 1/(4Bc)$  periodicity in time. Therefore, alignment revivals are expected to occur twice as often as orientation revivals.

### III. COMPUTATIONAL DETAILS

Details concerning the electronic-structure computations performed are described in this section. Readers who would like to skip this part should continue reading either at Subsection IV B, where the relationship of halogen substitution and the molecular parameters are explored, or at Section V, where the results of the laser-induced dynamics simulations are described.

The molecular parameters needed to solve Eq. (3) and to construct the matrix elements of Eq. (4), *i.e.*, the rotational constants (calculated with average atomic masses), the dipole moments, and the polarizabilities, were computed using either the CFOUR [45] or the MOLPRO [46] quantum-chemistry packages. The standard wave-function-theory quantum-chemical methods [41, 47, 48] employed include the restricted Hartree–Fock (RHF) method [49], its extension with electron correlation using second-order perturbation theory and the Møller–Plesset partitioning (MP2) [50, 51], coupled-cluster (CC) theory [52] with single and double excitations (CCSD) [53], and the gold-standard CCSD(T) method [54], whereby CCSD is augmented with a perturbative correction for triple excitations. We also performed computations within density-functional theory (DFT), employing the popular B3LYP functional [55–57].

The atom-centered, fixed-exponent Gaussian basis sets utilized during the electronic-structure computations have been developed by Dunning and co-workers [58]. The basis sets chosen include diffuse (aug) functions and occasionally the core-valence correlation is

also treated. We use the following abbreviations throughout the manuscript:  $XZ = \text{cc-pVXZ}$ ,  $\text{aXZ} = \text{aug-cc-pVXZ}$ ,  $\text{awcXZ} = \text{aug-cc-pwCVXZ}$ , and  $\text{awcXZpp} = [\text{aug-cc-pwCXZ}$  on the H and C atoms and  $\text{aug-cc-pwCXZ-pp}$  on the halogen atom,  $\text{pp} = \text{pseudopotential}]$ , where  $X$ , the cardinal number of the bases, is either 2(D), 3(T), 4(Q), or 5. For the analysis of the computed quantum-chemistry data, we apply the focal-point analysis (FPA) approach [59, 60]. FPA utilizes the fact that the increments of electronic energies and properties on the basis set size and the level of electron correlation are more-or-less independent from each other.

All directly computed molecular parameters correspond to the equilibrium structure. This becomes an issue when comparing directly computed (equilibrium) parameters to measured (effective) values, which are usually expectation values in the ground vibrational state [48]. Thus, besides the equilibrium values of the rotational constants ( $A_e$  and  $B_e$ ) and dipole moments ( $\mu_e$ ), their vibrationally averaged values ( $A_0$ ,  $B_0$ , and  $\mu_0$ ) were also computed for  $\text{CH}_3\text{F}$  and  $\text{CH}_3\text{Cl}$  at the  $\text{CCSD(T)}_{\text{-FC}}/\text{aug-cc-pVTZ}$  level, using the relative atomic weights of  $^1\text{H}$ ,  $^{12}\text{C}$ ,  $^{19}\text{F}$ , and  $^{35}\text{Cl}$ . The accurate  $A_0 - A_e$ ,  $B_0 - B_e$ , and  $\mu_0 - \mu_e$  differences can be used as corrections that can be added to equilibrium parameter values computed at different levels of electronic-structure theory. Vibrational corrections to the polarizability were not computed, because the expected effect is much smaller than the uncertainty in the experimental intensity values, most A&O simulations do not require very high accuracy for the polarizability (in contrast, laser-induced A&O dynamics is quite sensitive to the accuracy of the rotational constants (*vide infra*)). Highly accurate polarizability values that can be computed might become important in the future when the experimental intensity will be known more precisely.

During the A&O dynamics simulations employing the LIMA software, convergence of the simulated results with respect to the number of  $|JKM\rangle$  rotational basis functions and the cutoff value for the Boltzmann populations considered was ensured by gradually increasing and decreasing their values, respectively. An additional factor influencing A&O dynamics, through the populations of different rotational states and the rotational partition function, is the nuclear spin statistical weights (NSSW) of the different rotational levels. The  $\text{CH}_3\text{X}$  species are symmetric tops; thus, they belong to the  $D_\infty$  rotational symmetry group [44]. The NSSWs for the irreps of the  $D_\infty$  rotational symmetry group can be determined as prescribed by Bunker and Jensen [44] or the supplementary material of Ref. [40]. For all

the  $\text{CH}_3\text{X}$  molecules considered, they are as follows:  $\text{NSSW}^{\Sigma^+} = 2$ ,  $\text{NSSW}^{\Sigma^-} = 2$ ,  $\text{NSSW}^{E_1} = 1$ ,  $\text{NSSW}^{E_2} = 1$ , and  $\text{NSSW}^{E_3} = 2$ . These NSSWs reflect the relative abundance of the rotational states belonging to different irreps, which has to be considered when computing the thermal average of physical quantities, see Eq. (6). Note that the situation becomes different if different isotopologues are studied. Even though they have very similar electronic properties, different isotopologues should be treated as different species in terms of A&O dynamics, because the rotational constants and the NSSWs are different.

#### IV. ON MOLECULAR PARAMETERS IMPORTANT FOR A&O DYNAMICS

##### A. Effects of electron correlation and basis set size on molecular parameters

When the molecular parameters used in Eq. (4) are not available in the literature, their values can be computed with quantum-chemical methods. By using different Gaussian basis sets and electron-correlation methods in the electronic-structure computations, and by utilizing the principles of the FPA method [59, 60], the accuracy of the different computed molecular parameters and their impact on the dynamics calculations can be estimated. The  $\text{CH}_3\text{X}$  molecules chosen belong to the  $\text{C}_{3v}(\text{M})$  molecular symmetry group [44] and their equilibrium structures possess  $\text{C}_{3v}$  point-group symmetry. Thus, they are symmetric-top molecules, for which second-order tensorial properties can be divided into a parallel and perpendicular component, both with respect to the molecular symmetry axis. Tables I and II summarize the equilibrium molecular parameters most relevant for A&O simulations, computed at various levels of sophistication.

As Table I demonstrates, accurate determination of the molecular structures requires geometry optimizations carried out utilizing extensive basis sets as well as high-level treatment of electron correlation. For example, the basis-set-size increments in the equilibrium rotational constants moving from aug-cc-pVDZ (aDZ) to aug-cc-pVTZ (aTZ) at the RHF level is comparable to the correlation effect introduced by MP2. The next largest increments are from the more complete treatment of electron correlation at the CCSD and CCSD(T) levels, and increasing the basis set aTZ to aug-cc-pVQZ (aQZ). Accounting for core correlation, with the aug-cc-pwCVQZ (awcQZ) basis, seems to be necessary only to achieve very high accuracy. DFT (B3LYP) results are also included in Table I, showing that DFT, for this

TABLE I: Computed equilibrium rotational constants,  $A_e$  and  $B_e$ , and their method-dependent increments for the prolate symmetric-top  $\text{CH}_3\text{X}$  ( $\text{X} = \text{F}, \text{Cl}, \text{Br}, \text{I}$ ) species, all given in  $\text{cm}^{-1}$ , obtained at different levels of electronic-structure theory.

		$\text{CH}_3\text{F}$		$\text{CH}_3\text{Cl}$	
method <sup>a</sup>	basis <sup>a</sup>	$A_e$	$B_e$	$A_e$	$B_e$
RHF	DZ	5.2602	0.8762	5.2439	0.4410
	$\delta\text{aDZ}$	-0.0155	-0.0077	0.0008	-0.0010
	$\delta\text{aTZ}$	0.0860	0.0152	0.0896	0.0037
	$\delta\text{aQZ}$	0.0073	0.0015	0.0090	0.0015
	$\delta\text{a5Z}$	0.0013	0.0003	0.0030	0.0009
$\delta[\text{MP2}]$	aQZ	-0.0375	-0.0237	-0.0416	0.0041
$\delta[\text{CCSD}]$	aQZ	-0.0126	0.0057	-0.0102	-0.0028
$\delta[\text{CCSD(T)}]$	aQZ	-0.0208	-0.0066	-0.0229	-0.0023
CCSD(T)	$\delta\text{awcQZ}$	-0.0070	-0.0014	0.0040	0.0007
CCSD(T)	awcQZ	5.2602	0.8592	5.2725	0.4448
B3LYP	a5Z	5.2428	0.8516	5.2644	0.4394
		$\text{CH}_3\text{Br}$		$\text{CH}_3\text{I}$	
method <sup>a</sup>	basis <sup>a</sup>	$A_e$	$B_e$	$A_e$	$B_e$
CCSD(T)	awcQZ	5.2497	0.3210		
	awcQZpp			5.2371	0.2531

<sup>a</sup> ‘Method’ gives the electronic-structure technique used for the computation of the rotational constants. Increments are represented by the symbol  $\delta$ . When in front of a method given in brackets,  $\delta$  refers to the increment, obtained with the basis set specified under ‘basis’, with respect to the method preceding the indicated method in the following sequence:  $\text{RHF} \rightarrow \text{MP2} \rightarrow \text{CCSD} \rightarrow \text{CCSD(T)}$ . When  $\delta$  is in front of a basis set, the numerical values show the increment with respect to the basis set in the preceding line of the table. For the meaning of the basis-set abbreviations, see the text.

set of molecules and with the B3LYP functional, with a large basis set is a viable, inexpensive alternative to the sophisticated *ab initio* (wave-function-theory) methods if moderate accuracy suffices. In the case of  $\text{CH}_3\text{F}$ , the  $A_0 - A_e$  and  $B_0 - B_e$  vibrational corrections are  $-0.07688$  and  $-0.00813 \text{ cm}^{-1}$ , respectively. For  $\text{CH}_3\text{Cl}$ , the  $A_0 - A_e$  and  $B_0 - B_e$  corrections are  $-0.06692 \text{ cm}^{-1}$  and  $-0.00382 \text{ cm}^{-1}$ , respectively. These values are larger than the  $\delta[\text{CCSD(T)}]$  corrections.

Table II shows that, similar to that of the molecular structure, the most accurate dipole and polarizability values are obtained if large basis sets and theoretical methods accounting

for a substantial part of electron correlation are employed. This is due to the fact that the anisotropic charge distribution around the halogen nuclei play a crucial role in such molecules. The dipole-moment values seem to be much more sensitive to electron correlation than to basis-set size: the MP2 increment is more than ten(five) times larger than the increment from aug-cc-pwCVDZ (awcDZ) to aug-cc-pwCVTZ (awcTZ) at the RHF level for  $\text{CH}_3\text{F}(\text{CH}_3\text{Cl})$ . Nevertheless, going beyond the MP2/awcTZ level seems to be necessary only if accuracy beyond two digits is required. The polarizability values are, however, much more

TABLE II: Computed equilibrium molecular dipole ( $\mu_e$ ) and static polarizability ( $\alpha_{\parallel}$  and  $\alpha_{\perp}$ ) values and their increments for the  $\text{CH}_3\text{X}$  species, all in atomic units.

		$\text{CH}_3\text{F}$			$\text{CH}_3\text{Cl}$		
method <sup>a</sup>	basis <sup>a</sup>	$\mu_e$	$\alpha_{\parallel}$	$\alpha_{\perp}$	$\mu_e$	$\alpha_{\parallel}$	$\alpha_{\perp}$
RHF	awcDZ	0.8107	16.4172	15.1131	0.8421	34.3168	24.1080
	$\delta$ awcTZ	-0.0051	0.1448	0.2742	-0.0126	0.5703	0.8419
	$\delta$ awcQZ	-0.0017	0.0113	0.0602	-0.0020	0.0970	0.2324
	$\delta$ awc5Z	-0.0001	-0.0082	0.0053	0.0000	0.0111	-0.0048
$\delta$ [MP2]	awcQZ	-0.0628	1.2168	0.8114	-0.0659	0.7762	0.8749
$\delta$ [CCSD(T)]	awcQZ	-0.0044	-0.1128	-0.1028	-0.0070	-0.2378	-0.1372
CCSD(T)	awcQZ	0.7367	17.6773	16.1560	0.7546	35.5225	25.9200
B3LYP	a5Z	0.7330	18.360	16.853	0.7701	37.036	26.899
		$\text{CH}_3\text{Br}$			$\text{CH}_3\text{I}$		
method <sup>a</sup>	basis <sup>a</sup>	$\mu_e$	$\alpha_{\parallel}$	$\alpha_{\perp}$	$\mu_e$	$\alpha_{\parallel}$	$\alpha_{\perp}$
CCSD(T)	awcTZ	0.7266	44.4575	31.8600			
	$\delta$ awcQZ	0.0144	-0.0450	-0.0150			
CCSD(T)	awcQZpp				0.6592	58.9875	43.1250
$\delta$ [CCSD(T)+MVD1]	awcTZ	-0.0174	0.0400	0.0100			
	awcQZ	-0.0193	0.0775	0.0600			
	awcQZpp				0.0003	0.0175	0.0075
CCSD(T)+MVD1	awcQZ	0.7218	44.4900	31.9050			
	awcQZpp				0.6595	59.0050	43.1325

<sup>a</sup> ‘Method’ gives the electronic-structure technique used during the computation. Increments are represented by the  $\delta$  symbol. When in front of a method given in brackets,  $\delta$  refers to the increment, obtained with the basis set specified under ‘basis’, with respect to the method preceding the indicated method in the following sequence: RHF  $\rightarrow$  MP2  $\rightarrow$  CCSD(T) and CCSD(T)  $\rightarrow$  CCSD(T)+MVD1. When the  $\delta$  symbol is in front of a basis set, the numerical values show the increment with respect to the basis set in the preceding line of the table. For the meaning of the basis-set abbreviations, see the text.

sensitive to the size of the Gaussian basis. In these cases, the basis set increment from awcDZ to awcTZ is comparable to the MP2 increment, while the increment from awcTZ to awcQZ is comparable to the CCSD(T) increment. B3LYP with a large basis gives an accurate dipole for CH<sub>3</sub>F; however, the dipole of CH<sub>3</sub>Cl is significantly overestimated. B3LYP also fails to deliver accurate polarizabilities, as expected [48].

Relativistic effects might also be significant for heavy elements, because their inner electrons can have velocities comparable to the speed of light. Therefore, relativistic effects for the Br- and I-containing compounds were estimated by computing one-electron mass-velocity–Darwin (MVD1) [70–72] corrections. All-electron calculations were possible for CH<sub>3</sub>Br, showing MVD1 corrections comparable to the basis set increment from awcTZ to awcQZ, affecting the dipole and polarizability values in their second and third digits, respectively. For CH<sub>3</sub>I, the basis set describes core electrons with a pseudo potential, implicitly containing relativistic effects. Therefore, only frozen-core calculations were carried out, and, naturally, very small MVD1 corrections were obtained.

The  $\mu_0 - \mu_e$  difference computed at the CCSD(T)-FC/aug-cc-pVTZ level is  $-0.00548$  and  $-0.00813$  a.u. for CH<sub>3</sub>F and CH<sub>3</sub>Cl, respectively. These values are similar to the  $\delta[\text{CCSD(T)}]$  correction.

Finally, following the FPA protocol, the complete-basis-set (CBS) limit for the RHF dipole and polarizability values, as well as the CBS of their  $\delta[\text{MP2}]$  increment was extrapolated for all the CH<sub>3</sub>X molecules. In all occurrences we found that the CBS correction with respect to the awcQZ(pp) basis set is orders of magnitude smaller than the  $\delta[\text{CCSD(T)}]$  increment; therefore, the CBS values are not reported here, and the uncertainties of the best simulated values are estimated from above by the  $\delta[\text{CCSD(T)}]$  increment values.

## B. Substituent effects on chemical properties

Table III summarizes the equilibrium molecular properties computed as part of this work, obtained with the most sophisticated methods, CCSD(T) (+MVD1 for the dipole and polarizabilities of CH<sub>3</sub>Br and CH<sub>3</sub>I), and largest basis sets (awcQZ for CH<sub>3</sub>F, CH<sub>3</sub>Cl, and CH<sub>3</sub>Br; awcQZpp for CH<sub>3</sub>I) employed for the given molecule and property. These values were employed in the LMAO simulations. The vibrationally averaged rotational constants and dipole moments of CH<sub>3</sub>F and CH<sub>3</sub>Cl were computed by adding the computed  $A_0 - A_e$ ,

TABLE III: Recommended molecular parameters important for A&O processes: rotational constants ( $A_e$ ,  $B_e$ ,  $A_0$ , and  $B_0$ ), dipole moments ( $\mu_e$  and  $\mu_0$ ), and polarizabilities ( $\alpha_{\parallel}$ ,  $\alpha_{\perp}$ , and anisotropy,  $\Delta\alpha$ ) along with values of *experimental origin*, when available, given in parentheses below the results obtained within this study (CCSD(T)(+MVD1)/aug-cc-pwCVQZ(-pp) level, see text for details). Additional atomic and molecular properties shown are the carbon-halogen bond length,  $r_{C-X}$  (computed in this work), the van der Waals radius of the halogen atom,  $r_X$  [61], the electronegativity,  $EN_X$  [62], the first ionization energy,  $IE_X$  [62], the electron affinity,  $EA_X$  [62], and the atomic polarizability of the halogen atom,  $\alpha_X$  [63].

	CH <sub>3</sub> F	CH <sub>3</sub> Cl	CH <sub>3</sub> Br	CH <sub>3</sub> I
$A_e/\text{cm}^{-1}$	5.260 2 (5.265 00) <sup>a</sup>	5.272 5 (5.267 80) <sup>b</sup>	5.249 7 (5.246 31) <sup>c</sup>	5.237 1 (5.228) <sup>d</sup>
$B_e/\text{cm}^{-1}$	0.859 2 (0.859 84) <sup>a</sup>	0.444 8 (0.447 382) <sup>b</sup>	0.321 0 (0.321 92) <sup>c</sup>	0.253 1 (0.252 35) <sup>d</sup>
$A_0/\text{cm}^{-1}$	5.183 3 (5.182 00) <sup>e</sup>	5.205 6 (5.205 30) <sup>b</sup>		
$B_0/\text{cm}^{-1}$	0.851 1 (0.851 79) <sup>e</sup>	0.441 0 (0.443 40) <sup>b</sup>		
$\mu_e/\text{D}$	1.872 4	1.917 9	1.834 4	1.676 2
$\mu_0/\text{D}$	1.858 5 (1.85 $\pm$ 1%) <sup>f</sup>	1.897 2 (1.87 $\pm$ 1%) <sup>f</sup>	(1.81 $\pm$ 1%) <sup>f</sup>	(1.62 $\pm$ 2%) <sup>f</sup>
$\alpha_{\perp}/\text{\AA}^3$	2.394	3.841	4.728	6.392
$\alpha_{\parallel}/\text{\AA}^3$	2.620	5.264	6.593	8.744
$\Delta\alpha/\text{\AA}^3$	0.225	1.423	1.865	2.352
$r_{C-X}/\text{\AA}$	1.383	1.778	1.934	2.129
$r_X/\text{\AA}$	1.47	1.75	1.83	1.98
$EN_X$	3.98	3.16	2.96	2.66
$IE_X/\text{eV}$	17.423	12.968	11.814	10.451
$EA_X/\text{eV}$	3.401	3.613	3.364	3.059
$\alpha_X/\text{\AA}^3$	0.554(12)	2.163(15)	3.11(15)	4.88(19)

Sources of the experimental rotational constants: <sup>a</sup> Ref. 64, <sup>b</sup> Ref. 65, <sup>c</sup> Ref. 66, <sup>d</sup> Ref. 67, <sup>e</sup> Ref. 68.

<sup>f</sup> Source of the dipole moment corresponding to the ground vibrational state: Ref. 69. The experimental uncertainties reported include the variation due to the different vibrational states and different measurement techniques; therefore, they should cover the equilibrium values, as well.

$B_0 - B_e$ , and  $\mu_0 - \mu_e$  corrections to the equilibrium values. Table III also contains values



of experimental origin, from the literature [64–69, 73], along with some atomic properties taken also from the literature [62, 74]. As shown in Table III, there is a slight increase in the dipole moment going from  $\text{CH}_3\text{F}$  to  $\text{CH}_3\text{Cl}$ . On the other hand, due to the screening effect of the additional  $d$  orbitals, we see a decrease in the value of the dipole when moving from  $\text{CH}_3\text{Cl}$  to  $\text{CH}_3\text{I}$  [75]. In the case of the bond lengths and the polarizability values, a steady increase is observed from  $\text{CH}_3\text{F}$  to  $\text{CH}_3\text{I}$ , while the  $B_e$  rotational constant decreases in this order and  $A_e$  shows only a minor variation, in agreement with the changes in the structures of the prolate symmetric-top  $\text{CH}_3\text{X}$  species. As to the atomic properties, the electron affinity  $EA_X$  of the halogen atoms follows the trend shown by the molecular dipole [74, 75], the van der Waals radius  $r_X$  increases from F to I, while the electronegativity, ionization energy, and polarizability of the atom,  $EN_X$ ,  $IE_X$ , and  $\alpha_X$ , respectively, decrease in the same order.

Even though this work is limited to  $\text{CH}_3\text{X}$  molecules, our aim has been to arrive at conclusions as general as possible, in order to aid future work in designing and efficiently executing A&O-related research. We investigated, in this regard, the connection between molecular properties relevant in A&O processes and the chemical and physical properties of the test molecules or the atoms within. Thus, we calculated the correlation coefficient of  $\Delta\alpha$  and the dipole moment with the different atomic and molecular parameters (see

TABLE IV: Correlation of the polarizability anisotropy,  $\Delta\alpha$ , and the dipole moment,  $\mu_e$ , with various atomic and molecular parameters, denoted by  $\xi$ , for the four  $\text{CH}_3\text{X}$  molecules ( $X = \text{F}, \text{Cl}, \text{Br}, \text{and I}$ ).  $r_X$  = van der Waals radius,  $EN$  = electronegativity,  $IE$  = ionization energy, and  $EA$  = electron affinity. The correlation is denoted by  $\text{cor}(\Delta\alpha, \xi)$  and  $\text{cor}(\mu_e, \xi)$ . The correlation of  $X$  and  $Y$  quantities is calculated as  $\text{cor}(X, Y) = \langle X - \langle X \rangle \rangle \langle Y - \langle Y \rangle \rangle / (\sigma_X \sigma_Y)$ , where  $\langle \rangle$  denotes the expectation value, and  $\sigma_X, \sigma_Y$  denote the standard deviation of  $X$  and  $Y$ , respectively. The sample-size-adjusted correlation coefficient,  $\text{cor}^* = \text{sgn}(\text{cor}) (|\text{cor}| - 0.95) / 0.05$  (where  $\text{sgn}$  is the sign function) is computed for the statistically significant correlations, meaning  $|\text{cor}| > 0.95$  (see text for details). Large  $\text{cor}^*$  values are boldfaced, indicating strong linear relationship.

$\xi$	$\text{cor}(\Delta\alpha, \xi)$	$\text{cor}^*(\Delta\alpha, \xi)$	$\text{cor}(\mu_e, \xi)$	$\text{cor}^*(\mu_e, \xi)$
$\mu_e$	-0.666		1.000	1.000
$\alpha_\perp$	0.965	0.302	-0.835	
$\alpha_\parallel$	0.985	0.705	-0.782	
$\Delta\alpha$	1.000	1.000	-0.666	
$r_{\text{C-X}}$	0.999	<b>0.981</b>	-0.697	
$r_X$	1.000	<b>0.992</b>	-0.682	
$EN_X$	-0.998	<b>-0.955</b>	0.625	
$IE_X$	-0.997	<b>-0.931</b>	0.604	
$EA_X$	-0.525		0.977	0.538
$\alpha_X$	0.968	0.368	-0.828	

Table IV). The seemingly large correlation coefficients found can be misleading because the number of data points is low (there are only four molecules), so uncorrelated quantities can accidentally have large correlation coefficients. In the case of four data points, if the absolute value of the correlation coefficient ( $\text{cor}$ ) is larger than 0.95, then the probability of an accidental correlation is only 5% [76]. Thus, we also calculated the sample-size-adjusted correlation coefficient,  $\text{cor}^* = \text{sgn}(\text{cor})(|\text{cor}| - 0.95)/0.05$  (where  $\text{sgn}$  is the sign function), to measure the correlation above the threshold value of 0.95, and indicated the large  $\text{cor}^*$  values with boldfaced numbers in Table IV.

Based on the data of Table IV, one can see that there is a strong linear relationship between  $\Delta\alpha$  and the carbon-halogen bond length ( $r_{\text{C-X}}$ ) and the van der Waals radius ( $r_{\text{X}}$ ), while there is a negative correlation with the electronegativity and the ionization energy. Polarizability is usually assumed to be nearly proportional to the molecular volume; therefore, the linear dependency of  $\Delta\alpha$ , the polarizability anisotropy, on the radius of the halogen atom is somewhat surprising, especially in the light of the rigorous relation between the volume and the static polarizability of quantum systems revealed [77]. The linear dependency is probably caused by the very small sample size, and one should not draw serious conclusions from this. Nonetheless, we find that the larger the molecular volume, the larger the polarizability. For a set of molecules with similar, non-spherical structure this translates to larger volumes leading to larger polarizability anisotropies. The dipole moment shows significant correlation with the electron affinity of the halogen. It is important to note that among the quantities investigated here, the dipole moment and the electron affinity are the only non-monotonous functions of the atomic number of the halogen. Note that the dipole moment varies much less than the other chemical properties, probably because the partial charge, depending on the electronegativity difference between the carbon and the halogen atoms, decreases with the size of the halogen, but  $r_{\text{C-X}}$  increases, increasing the separation of the partial charges, and these opposite effects tend to cancel each other in the dipole moment.

## V. SINGLE-OPTICAL-PULSE ALIGNMENT

In this section we are investigating the single-optical-pulse alignment dynamics of the  $\text{CH}_3\text{X}$  species, for medium- to high-intensity ( $1\text{--}30\text{ TWcm}^{-2}$ ) femtosecond pulses, which

can be generated by tabletop Ti:sapphire setups [78] or those available at dedicated institutes [28]. We are studying the effect of molecular parameters, such as rotational constants, polarizability, and the contribution from different irreps of the rotation group to the alignment, as well as the sensitivity of the alignment to the accuracy of these parameters. For the sake of completeness, we also investigate the effects of experimental conditions, *i.e.*, the temperature and pulse parameters.

### A. The role of different molecular parameters

First, let us investigate the effect of the change of substituent on A&O dynamics in the case of optical pulses ( $\lambda = 800$  nm is chosen). If the temperature and the laser parameters are kept fixed, the rotational constants and the polarizability anisotropy ( $\Delta\alpha$ ) determine the A&O dynamics. The rotational constants determine the time of the rotational revivals and the maximal alignment: heavier molecules, with smaller  $B_e$  rotational constants, have

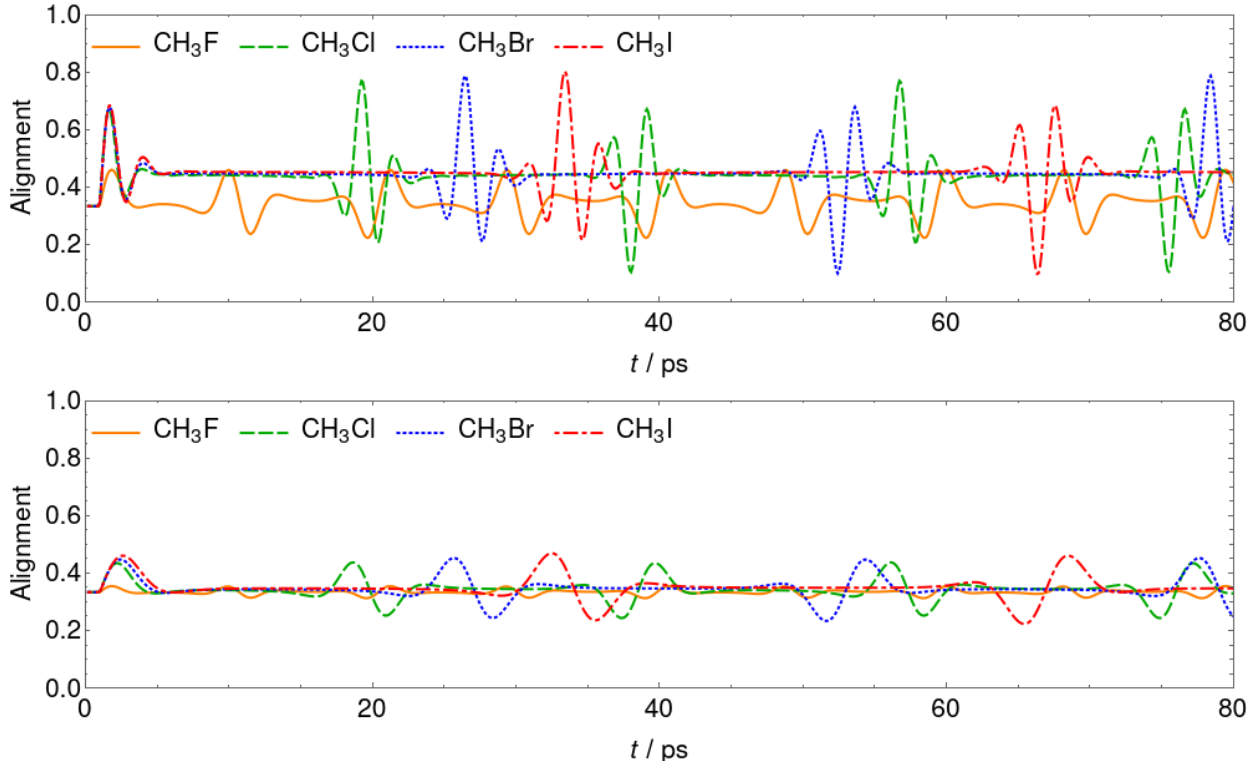


FIG. 1: Comparison of the laser-induced rotational alignment of the  $\text{CH}_3\text{X}$  molecules for a medium- and a high-intensity optical pulse. The pulse parameters chosen are as follows:  $T/\text{K} = 5$ ,  $\lambda/\text{nm} = 800$ ,  $I/\text{TW cm}^{-2} = 30$  (upper panel) and 5 (lower panel),  $\text{FWHM}/\text{fs} = 100$ , and the pulse position is 1 ps.

longer rotational periods and smaller maximal alignment than the lighter molecules. This is due to more initial rotational states being populated at the given temperature (*vide infra*). Increasing the polarizability anisotropy increases the maximal alignment due to the higher degree of excitation, as shown below. For the  $\text{CH}_3\text{X}$  series, the rotational constants are decreasing with the size of the halogen, while the polarizability anisotropy is increasing:  $\Delta\alpha_{\text{CH}_3\text{F}} < \Delta\alpha_{\text{CH}_3\text{Cl}} < \Delta\alpha_{\text{CH}_3\text{Br}} < \Delta\alpha_{\text{CH}_3\text{I}}$ , with the largest difference found between  $\text{X} = \text{F}$  and  $\text{Cl}$ . Thus, it is expected that increasing the size of the halogen increases the time between the revivals and increases the maximal alignment.

For optical pulses, the dipole moment has no effect on A&O dynamics, because the field-dipole interaction averages out to zero during the fast oscillation of the field [42]. This is also a reason why nonzero orientation cannot be achieved using a single optical pulse. This was tested by comparing converged simulations explicitly including the dipole interaction with simulations utilizing the cycle-averaging approximation [40, 42], when the dipole interaction is neglected and only the envelope of the pulse is considered. The two cases show identical alignment curves and no orientation.

Fig. 1 shows the results computed for  $T = 5$  K for two different pulse intensities, 5  $\text{TW cm}^{-2}$  (lower panel) and 30  $\text{TW cm}^{-2}$  (upper panel), with a  $\lambda = 800$  nm Gaussian pulse positioned to 1 ps and having a full width half maximum (FWHM) of 100 fs. The alignment curves of the four molecules are clearly different, but similarities can also be identified. For the pulse with the larger intensity, the curve of  $\text{CH}_3\text{F}$  stands out with its lower base level and a reduced maximal alignment, while for the other three molecules the maximal alignments are quite similar, only the revival periods are different. We can achieve only a much smaller alignment with the lower intensity pulse, and the revival peaks of  $\text{CH}_3\text{F}$  become smaller relative to the other three molecules. The half-revival time periods,  $T_{\text{rev}} = 1/(4cB_e)$ , are 9.71, 18.75, 25.98, and 32.95 for  $\text{CH}_3\text{F}$ ,  $\text{CH}_3\text{Cl}$ ,  $\text{CH}_3\text{Br}$ , and  $\text{CH}_3\text{I}$ , respectively. Based on the periodicity and the alternating polarity of the revivals, these are all  $J$ -type revivals [22], where the molecule rotates around the  $b$  and  $c$  molecular axes. When compared to experimental laser-induced alignment curves, our simulations exhibit agreement in terms of revival times and the shape of the revival curves; for examples, see Fig. 1 of Ref. 37 for  $\text{CH}_3\text{Cl}$ , Fig. 3 of Ref. 38 for  $\text{CH}_3\text{Br}$ , and Fig. 2 of Ref. 35, Fig. 4 of Ref. 36 and Fig. 4 of Ref. 38 for  $\text{CH}_3\text{I}$ . Note that the exact measure of alignment and the experimental parameters are different from those in our simulations; therefore, the measured and computed alignment

curves cannot be compared directly.

### 1. The role of polarizability anisotropy

Next, let us investigate the relative effects of the rotational constant and the polarizability. To pinpoint the role of the polarizability anisotropy on laser-induced rotational alignment, simulations were performed for all molecules, whereby the rotational constants were fixed to the value corresponding to  $\text{CH}_3\text{F}$ . The computed alignment dynamics, shown in Fig. 2, confirm that the periodicity of the revivals is determined by the rotational constants, while the maximal alignment is governed by the polarizability. In the lower panel of Fig. 2, corresponding to the low-intensity-pulse scenario, the  $\text{CH}_3\text{F}$  curve stands out with its very small oscillation amplitude, but the peak heights for the different molecules reflect the relative values of their polarizability anisotropy. In the case of the high-intensity pulse (upper panel of Fig. 2),  $\text{CH}_3\text{F}$  stands out even more with a considerably lower baseline and

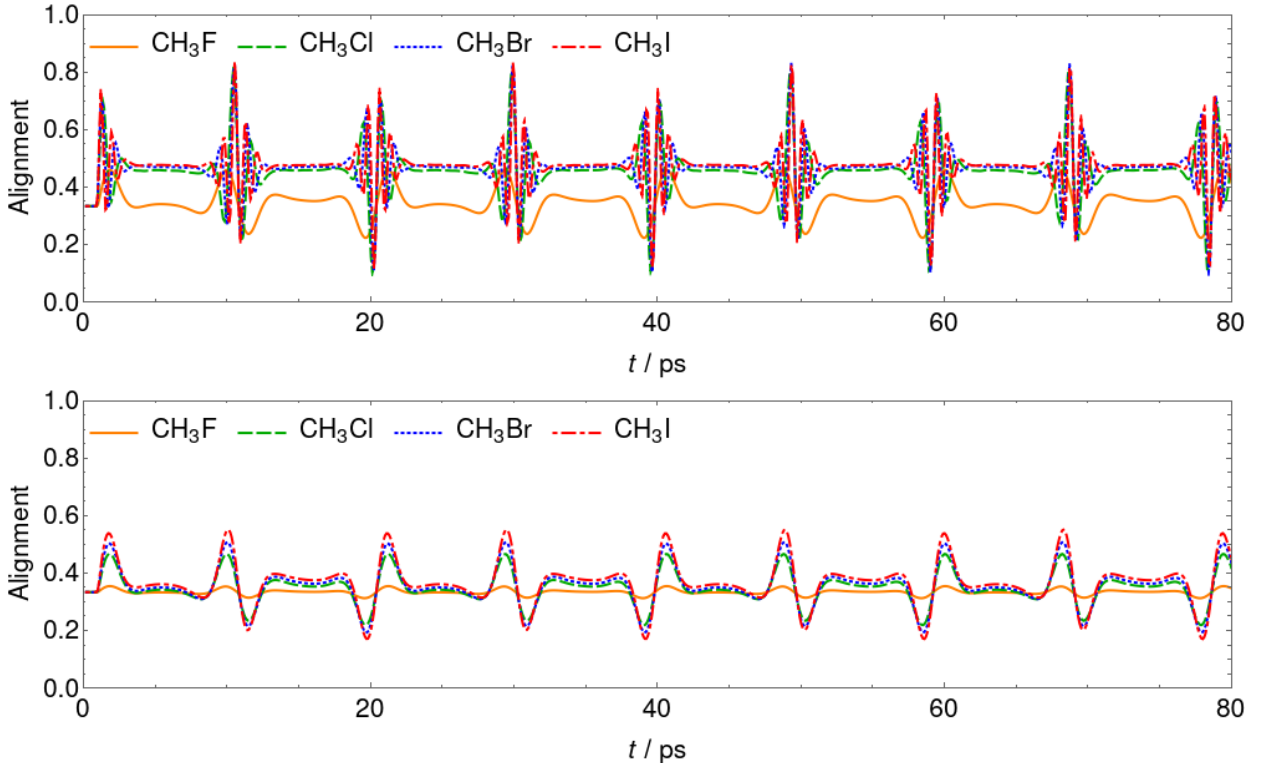


FIG. 2: Testing the effect of polarizability anisotropy on laser-induced rotational alignment, by setting the rotational constant to the corresponding value of  $\text{CH}_3\text{F}$  for all four molecules. The pulse parameters chosen are as follows:  $T/\text{K} = 5$ ,  $\lambda/\text{nm} = 800$ ,  $I/\text{TW cm}^{-2} = 30$  (upper panel) and 5 (lower panel),  $\text{FWHM}/\text{fs} = 100$ , and the pulse position is 1 ps.

reduced rotational excitation, similar to Fig. 1. The other three molecules show very similar curves in the high-intensity scenario, indicating that the differences in their polarizability has a smaller effect on the alignment at high pulse intensity than at low intensity, due to the saturation of the excitation.

## 2. The role of rotational constants

The effect the rotational constants have on A&O dynamics was studied by simulations in which the polarizabilities were fixed to the values corresponding to  $\text{CH}_3\text{Cl}$  for all molecules. The results, shown in Fig. 3, demonstrate that the rotational constants not only determine the rotational revival times, but also affect the alignment maxima, which slightly decrease with the size of the halogen atom. This behavior can be explained by the increase in the number of rotational states having significant Boltzmann populations as the size of the halogen atom is increased (*i.e.*, the smallest rotational constant is decreased), see Table

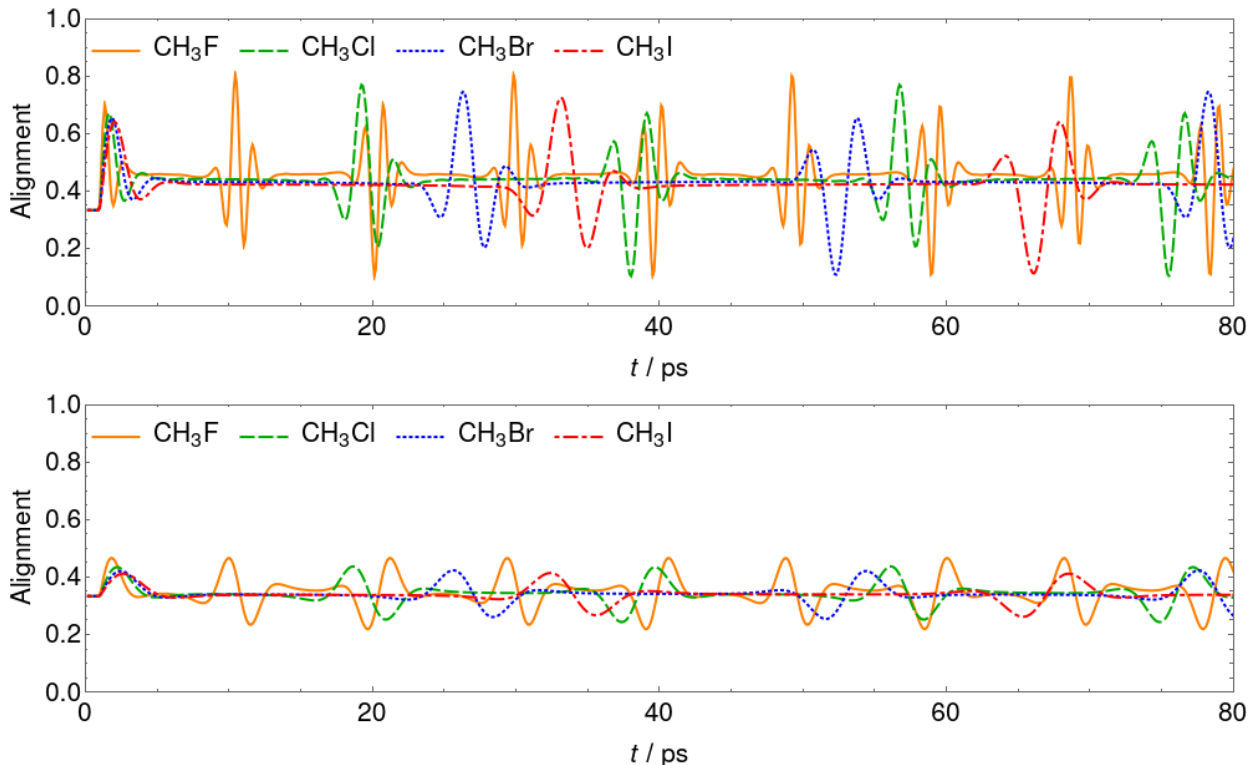


FIG. 3: Testing the effect of rotational constants on laser-induced rotational alignment. For all molecules, the polarizability is fixed to values corresponding to  $\text{CH}_3\text{Cl}$ . The pulse parameters chosen are as follows:  $T/\text{K} = 5$ ,  $\lambda/\text{nm} = 800$ ,  $I/\text{TW cm}^{-2} = 30$  (upper panel) and 5 (lower panel),  $\text{FWHM}/\text{fs} = 100$ , and the pulse position is 1 ps.

V below. The differences in the maximal alignments are more pronounced for the lower intensity pulse, which indicates a saturation effect in the alignment with respect to the laser-pulse intensity, as detailed below in Sec. V B 1. Based on the results obtained by either fixing the rotational constant or the polarizability to the same value for all molecules, we can conclude that these two parameters have an opposite effect to the maximal alignment with respect to the size of the halogen atom, but the effect of the polarizability dominates, especially at high intensities.

### 3. Sensitivity to the accuracy of molecular parameters

In this section we present our results on the effects of molecular parameter accuracy on the laser-induced rotational alignment. Tables I and II contain the equilibrium molecular parameters of  $\text{CH}_3\text{F}$  and  $\text{CH}_3\text{Cl}$  computed at different levels of electronic-structure theory utilizing various basis sets, while Table III contains the  $A_0$  and  $B_0$  parameters. Figure 4 shows the laser-induced rotational alignment of  $\text{CH}_3\text{F}$  and  $\text{CH}_3\text{Cl}$  obtained with parameters computed at the best, aug-cc-pwCVQZ CCSD(T), level and at the much less expensive aug-cc-pV5Z B3LYP level. The alignment dynamics obtained with the  $A_0$  and  $B_0$  rotational constants almost coincides with the related B3LYP curve. This is due to the fact that  $B_0$  is very close to  $B_{\text{e,a5Z B3LYP}}$ . This agreement is only a coincidence, as  $A_{\text{e,a5Z B3LYP}}$  is closer to  $A_{\text{e,awcQZ CCSD(T)}}$  than to  $A_0$ . The maximal alignments obtained with the different parameter sets are very similar to each other but the revivals are drifting away with increasing time. This indicates that it is crucial to use very accurate rotational constants in LIMA0 simulations. The accuracy of the polarizability tensor is much less important, because it has only a minor effect on the alignment and the intensity is not known very precisely in the experiments.

### 4. The role of symmetry and nuclear spin statistical weights

The selection rules of the laser-induced rotational transitions are determined by symmetry [44]. The polarizability of the  $\text{CH}_3\text{X}$  species transforms as  $\Sigma^+$ , the totally symmetric irreducible representation (irrep) of the  $D_\infty$  rotation group. The polarizability transition between states  $i$  and  $f$ , belonging to the  $\Gamma_i$  and  $\Gamma_f$  irreps, respectively, is allowed if

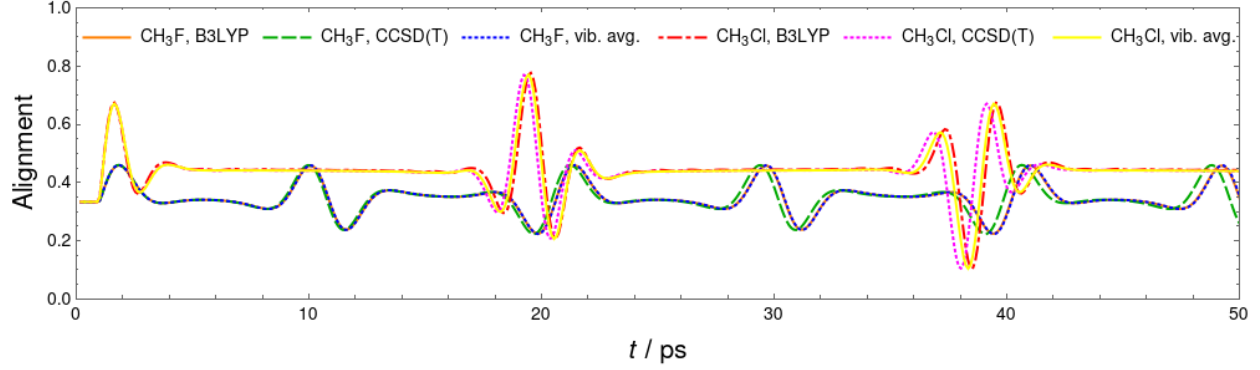


FIG. 4: Testing the effect of parameter accuracy on the laser-induced rotational alignment of  $\text{CH}_3\text{F}$  and  $\text{CH}_3\text{Cl}$ . The ‘B3LYP’ and ‘CCSD(T)’ curves correspond to using equilibrium molecular parameters obtained at the aug-cc-pV5Z B3LYP and aug-cc-pwCVQZ CCSD(T) levels, respectively (see Tables I and II), while the ‘vib. avg.’ curves, which coincide with the ‘B3LYP’ curves, were obtained using rotational constants  $A_0$  and  $B_0$  (see Table III). The pulse parameters chosen are as follows:  $T/\text{K} = 5$ ,  $\lambda/\text{nm} = 800$ ,  $I/\text{TW cm}^{-2} = 30$ ,  $\text{FWHM}/\text{fs} = 100$ , and the pulse position is 1 ps.

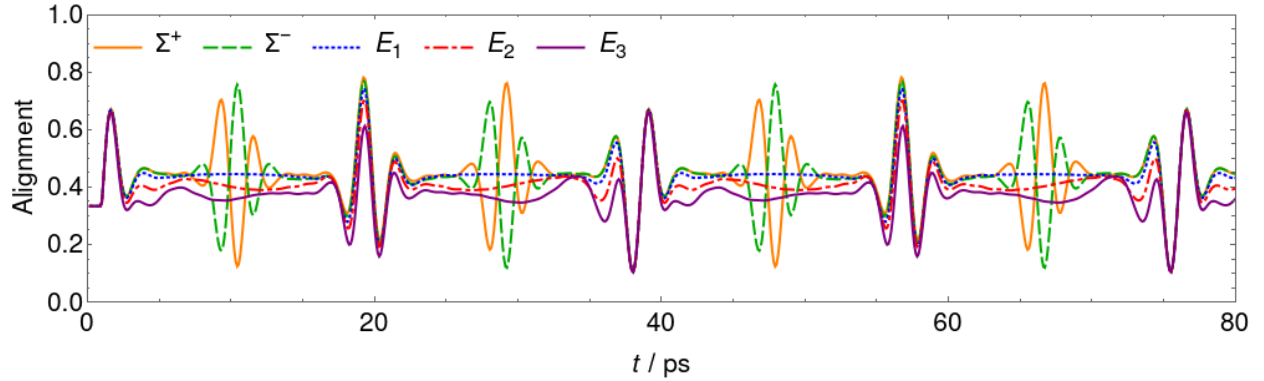


FIG. 5: Testing the contribution of the rotational states belonging to each irrep of the  $D_\infty$  rotational symmetry group to the alignment of  $\text{CH}_3\text{Cl}$ . This is based on the selection rules for the optical pulse, which allow transitions only within a given irrep. The pulse parameters chosen are as follows:  $T/\text{K} = 5$ ,  $\lambda/\text{nm} = 800$ ,  $I/\text{TW cm}^{-2} = 30$ ,  $\text{FWHM}/\text{fs} = 100$ , and the pulse position is 1 ps.

$\Sigma^+ \subseteq \Gamma_f \otimes \Sigma^+ \otimes \Gamma_i = \Gamma_f \otimes \Gamma_i$ . Thus, based on the product table of the  $D_\infty$  group [73], the polarizability transitions are only allowed between states belonging to the same irrep.

In order to study the contribution of the rotational states belonging to each irrep to the alignment of  $\text{CH}_3\text{Cl}$ , we made simulations where the NSSW was 1 for a single irrep and 0 for the others. The results can be seen in Fig. 5. Rotational states belonging to the  $E_1$ ,  $E_2$ ,  $E_3$  irreps produce revivals at every  $nT_{\text{rev}}$  ( $n \in \mathbb{N}$ ), while  $\Sigma^+$  and  $\Sigma^-$  has revivals at every  $(n + 1/2)T_{\text{rev}}$ , as well, but these cancel each other out when all irreps are included in the



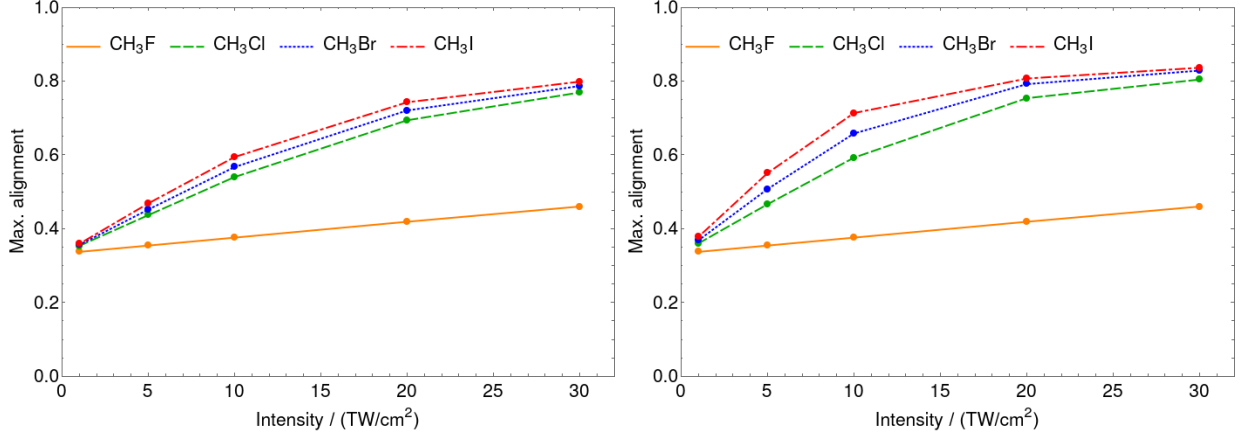


FIG. 6: Left panel: The maximal alignment as a function of pulse intensity for the  $\text{CH}_3\text{X}$  molecules at 5 K. Right panel: same as left panel, but the rotational constants are fixed to the  $\text{CH}_3\text{F}$  value for all molecules. The pulse parameters chosen are as follows:  $T/\text{K} = 5$ ,  $\lambda/\text{nm} = 800$ ,  $\text{FWHM}/\text{fs} = 100$ , and the pulse position is 1 ps.

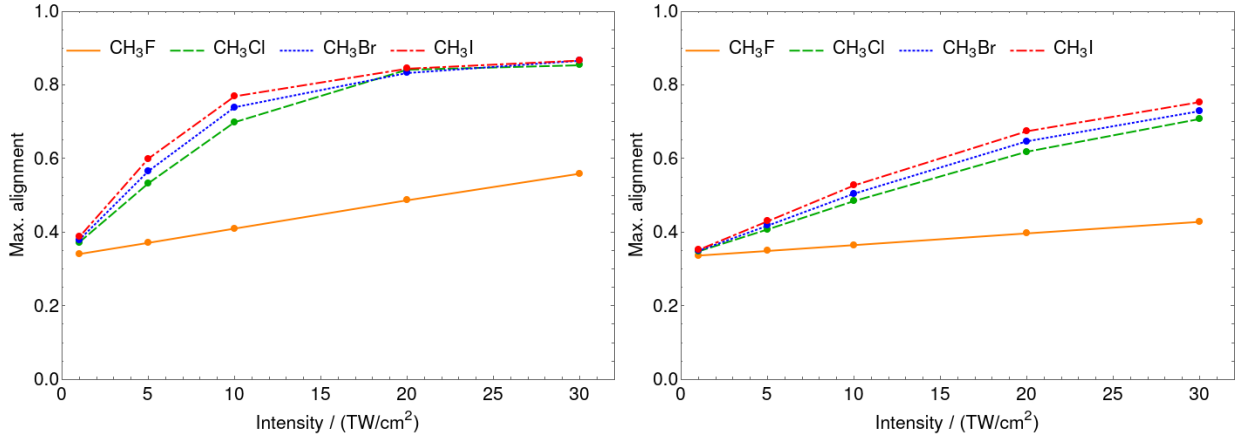


FIG. 7: The maximal alignment as a function of pulse intensity for the  $\text{CH}_3\text{X}$  molecules at 1 K (left panel) and 10 K (right panel). The pulse parameters chosen are as follows:  $\lambda/\text{nm} = 800$ ,  $\text{FWHM}/\text{fs} = 100$ , and the pulse position is 1 ps.

simulation.

## B. The role of experimental parameters

### 1. Pulse energy

For the sake of completeness, we briefly discuss the effect of experimental parameters on the alignment of  $\text{CH}_3\text{X}$  molecules. Figure 6 shows the maximal alignment as a function of the pulse intensity between 1 and 30  $\text{TW cm}^{-2}$  at 5 K. The  $\text{CH}_3\text{F}$  molecule clearly stands

out (as also apparent from the previous sections), because it has a linear response in this intensity range, while the behavior of the other three molecules are nonlinear, similar in shape, and produce a saturation-type curve.

The question is whether this saturation-type behavior is a consequence of the different Boltzmann populations or the different polarizabilities. Repeating the above calculation while fixing the rotational constants of all molecules to that of the  $\text{CH}_3\text{F}$  value (see the right panel of Fig. 6) resulted in a roughly similar plot, which again stresses that  $\text{CH}_3\text{F}$  stands out because of its much smaller polarizability anisotropy.

## 2. Temperature

As the atomic weight of the halogen atom and the  $r_{\text{C-X}}$  carbon-halogen bond length increase from F to I, the moments of inertia along the axes perpendicular to the C–X bond increase, as well. This results in the decrease of the respective rotational constants, leading to an increased density of rotational states. Therefore, at finite temperatures the number of rotational states with non-negligible Boltzmann population will increase in succession from F to I, which is reflected in the values of the rotational partition functions.

Indeed, as summarized in Table V, the value of  $Q_{\text{rot}}(T)$  increases and the population of the  $J = 0$  state decreases when the atomic weight of X (from F to I) increases, *i.e.*, the heavier the substituent, the more care is needed to account for all populated rotational states. With more rotational states having non-negligible Boltzmann population, a more pronounced effect of thermal averaging on the A&O dynamics should be expected, resulting in lower maximal alignment. Figure 7 shows the maximal alignment as a function of the pulse intensity between 1 and 30  $\text{TW cm}^{-2}$  at 1 K and 10 K. The 10 K case exhibits somewhat lower alignment values than those of Fig. 6, corresponding to 5 K, while for 1 K, the alignment is higher and the saturation starts at lower intensities.

## VI. SINGLE-THZ-PULSE ALIGNMENT AND ORIENTATION

In this section the rotational dynamics of the  $\text{CH}_3\text{X}$  species is investigated when the molecules are excited by a single intense THz pulse, causing non-adiabatic A&O dynamics. Similar to the case of the optical pulse, we study the effect of molecular parameters and the

TABLE V: Rotational partition function ( $Q_{\text{rot}}(T)$ ) and population of the  $J = 0$  ground state ( $p(J = 0)$ ) at temperatures of 0 K, 0.1 K, and 5 K

molecule	$Q_{\text{rot}}(T)$			$p(J = 0)$		
	$T = 0$ K	$T = 0.1$ K	$T = 5$ K	$T = 0$ K	$T = 0.1$ K	$T = 5$ K
CH <sub>3</sub> F	2	2	11.18811	1	1	0.179
CH <sub>3</sub> Cl	2	2.00003	20.76103	1	1	0.096
CH <sub>3</sub> Br	2	2.00076	28.31901	1	1	0.071
CH <sub>3</sub> I	2	2.00491	32.62516	1	0.998	0.061

sensitivity of A&O to the accuracy of these parameters. The effects of the pulse parameters are investigated, as well, during which the regime of adiabatic A&O dynamics is also explored.

#### A. The role of pulse parameters, adiabatic and non-adiabatic regimes

The first set of pulse parameters used in our simulations reflect realistic values available at the ELI-ALPS institute [28]:  $\nu = 0.333$  THz (equivalent to  $11.1 \text{ cm}^{-1}$  wavenumber) or  $0.25$  THz (equivalent to  $8.3 \text{ cm}^{-1}$  wavenumber),  $I = 5 \times 10^{-4} \text{ TW cm}^{-2}$ , FWHM = 2000 fs, and CEP =  $\pi/2$ , where CEP stands for carrier envelope phase. In the case of THz pulses, the field-dipole interaction becomes dominant, because the polarizability interaction is proportional to the square of the electric field and the intensity is much lower than it was for the optical pulses. Furthermore, contrary to the optical-pulse case, the electric-field oscillation is slow enough for the field-dipole interaction not to average out to zero (cycle averaging can not be used), which can lead to orientation in addition to alignment. As presented in Figs. 8 and 9, such THz pulses can produce significant alignment and orientation for CH<sub>3</sub>F, with smaller effect for the other molecules. The order of maximal orientation and alignment is CH<sub>3</sub>F > CH<sub>3</sub>Cl > CH<sub>3</sub>Br > CH<sub>3</sub>I. In accordance with Section II, the alignment revivals are alternating and have the same time period as in the single-optical pulse case, while the orientation revivals do not alternate and occur twice as seldom.

The maximal alignment and orientation is larger for the 0.25 THz pulse than for the 0.333 THz pulse, because the photon energy of the former is closer to the rotational transitions determined by the  $B_e$  rotational constants (see Table III).

The *adiabatic* regime of the A&O dynamics was also studied by varying the THz pulse parameters. We chose CH<sub>3</sub>F for this investigation, because the other molecules would pro-

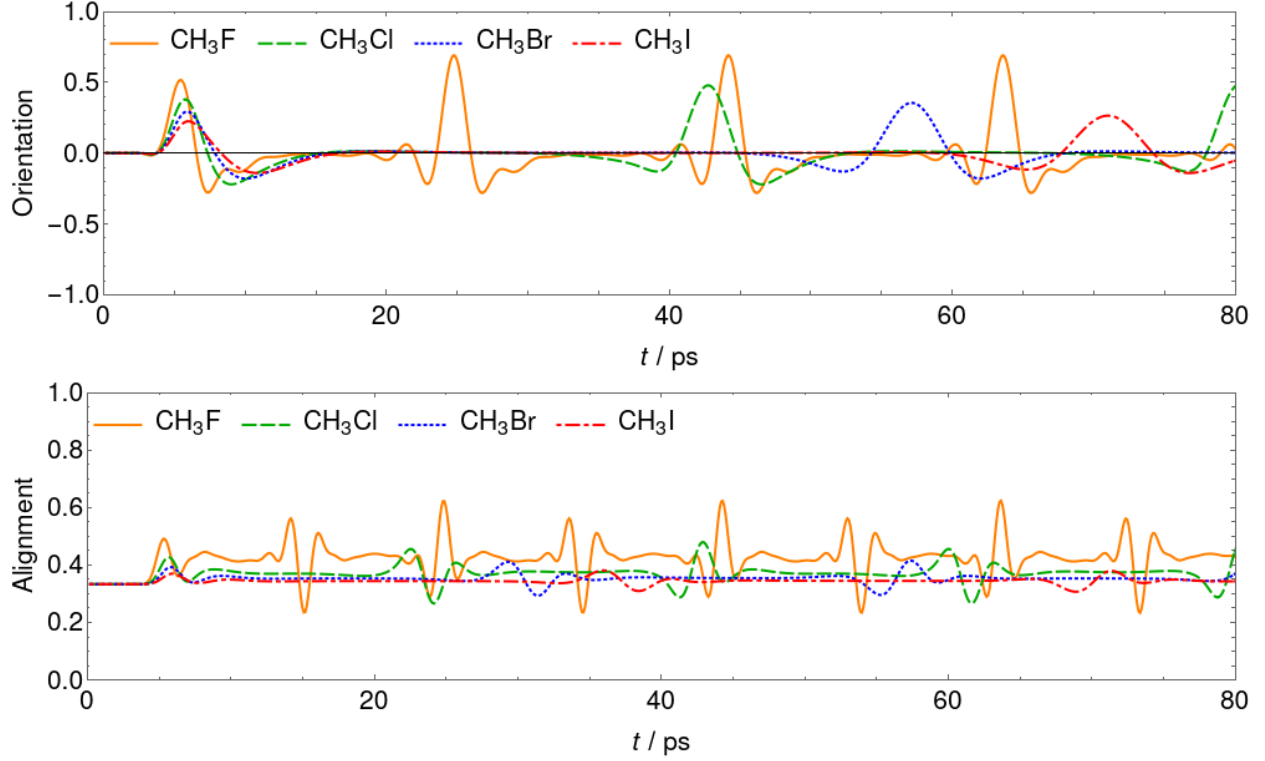


FIG. 8: Alignment and orientation dynamics of the  $\text{CH}_3\text{X}$  molecules following a THz-pulse excitation with pulse parameters of  $T/\text{K} = 5$ ,  $\nu/\text{THz} = 0.25$ ,  $\text{FWHM}/\text{fs} = 2000$ ,  $I/\text{TW cm}^{-2} = 5 \times 10^{-4}$ , pulse position at 5 ps, and  $\text{CEP} = \pi/2$ .

vide much smaller adiabatic A&O. *Non-adiabatic alignment or orientation* is observed when the laser pulse is turned on (and/or off) much faster than the rotational period(s). In this case the molecule shows time-dependent revivals under field-free conditions, long after the laser pulse disappeared. In the case of *adiabatic alignment or orientation*, the laser pulse is turned on (and off) much slower than the rotational period(s). In this case the spatial order of the molecules exists only during the pulse. Figure 10 shows how the orientation for  $\text{CH}_3\text{F}$  is affected by the frequency, duration, and intensity of the pulse. The intensity and the duration of the pulse were varied such that  $I \times \text{FWHM}$  was kept constant. The tested frequencies are 0.5, 0.25, and 0.167 THz, the intensity values are  $5 \times 10^{-4}$ ,  $1 \times 10^{-4}$ , and  $5 \times 10^{-5} \text{ TW cm}^{-2}$ , while 2, 10, and 20 ps are used for the FWHM. One can see that the  $\text{FWHM} = 2 \text{ ps}$  case is clearly non-adiabatic, because the pulse is much shorter than the characteristic timescale of rotational motion, but for the cases of  $\text{FWHM} = 10$  and  $20 \text{ ps}$ , we are entering the adiabatic regime, though the maximal orientation significantly decreases (note that the range of the vertical axis is only  $[-0.5, 0.5]$ ). In this case, the molecular orientation

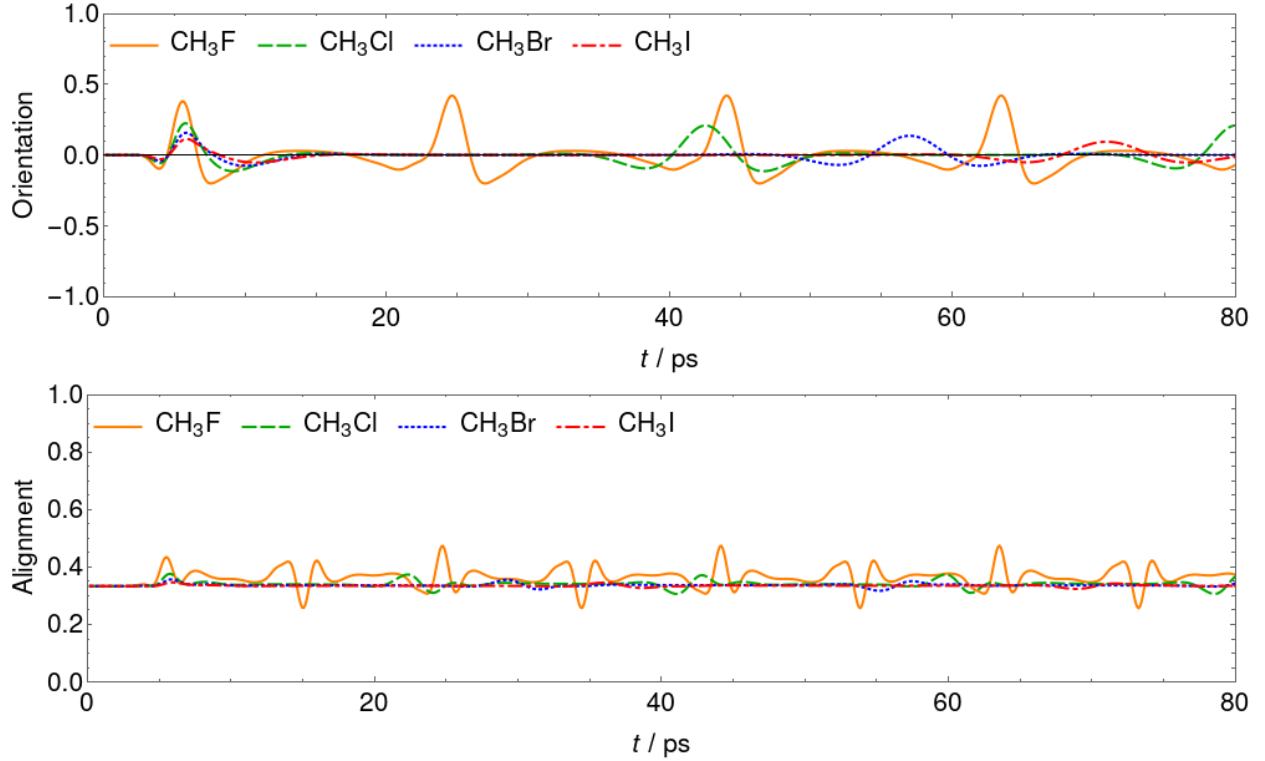


FIG. 9: Alignment and orientation dynamics of the  $\text{CH}_3\text{X}$  molecules following a THz-pulse excitation with pulse parameters of  $T/\text{K} = 5$ ,  $\nu/\text{THz} = 0.333$ ,  $\text{FWHM}/\text{fs} = 2000$ ,  $I/\text{TW cm}^{-2} = 5 \times 10^{-4}$ , pulse position at 5 ps, and  $\text{CEP} = \pi/2$ .

follows the oscillation of the electric field during the pulse, but revivals are still present after the pulse, so the situation is not completely adiabatic. Out of the curves shown in Fig. 10, the  $\nu = 0.25$  THz and  $\text{FWHM} = 10$  ps case is the closest to the adiabatic situation, but the achieved orientation is only moderate. The maximal orientation decreases if the frequency is increased, because the frequency is moved further from the rotational transitions, so the excitation decreases. Fig. 10 demonstrates that for a given frequency, increasing the pulse duration also decreases the orientation and the degree of excitation, because the bandwidth of the pulse becomes narrower, and less resonant with the rotational transitions.

## B. The role of molecular parameters

### 1. Rotational constants, dipole moment, and polarizability

The computations summarized in Figs. 8 and 9 were repeated after setting the polarizabilities to zero for all four molecules, which did not change the results within numerical

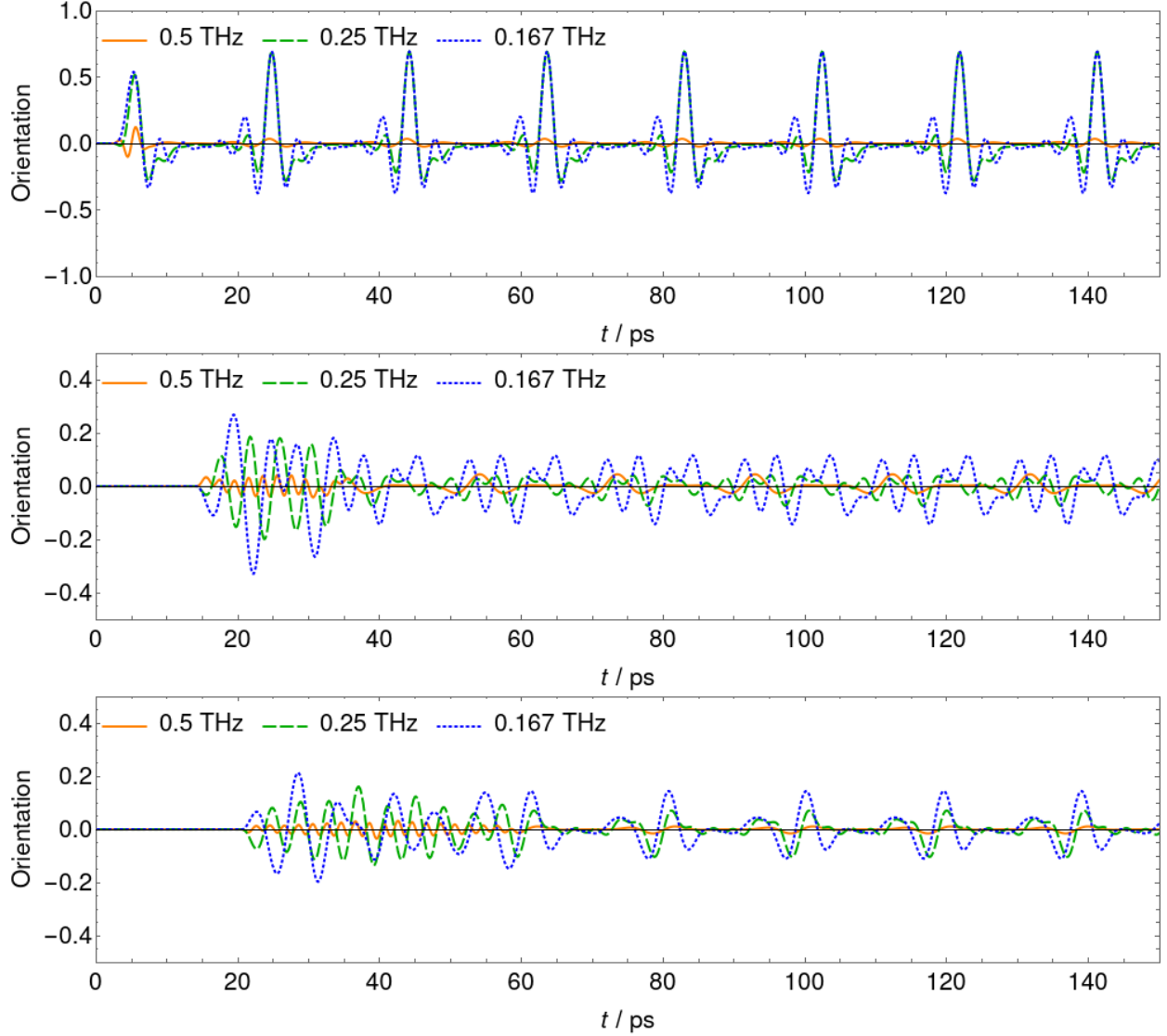


FIG. 10: Effect of THz pulse parameters on the orientation of  $\text{CH}_3\text{F}$ . The frequency ( $\nu$ ), intensity ( $I$ ), and FWHM was varied, keeping the total pulse energy,  $I \times \text{FWHM}$  constant.  $T/\text{K} = 5$  and  $\text{CEP} = \pi/2$  were used for all panels. The other pulse parameters of the top panel:  $\text{FWHM} = 2$  ps,  $I = 5 \times 10^{-4} \text{ TW cm}^{-2}$ , pulse position was 5 ps; middle panel:  $\text{FWHM} = 10$  ps,  $I = 1 \times 10^{-4} \text{ TW cm}^{-2}$ , pulse position was 25 ps; bottom panel:  $\text{FWHM} = 20$  ps,  $I = 5 \times 10^{-5} \text{ TW cm}^{-2}$ , pulse position was 40 ps.

error. Therefore, the polarizability interaction with the field is negligible in this situation, as expected at such low field intensity. To clarify the different THz pulse-induced rotational behavior of the  $\text{CH}_3\text{X}$  species and the role of the rotational constants, simulations with zero polarizability and an equal dipole of 2 D for all molecules were carried out. (in fact, the dipole moment is quite similar for all molecules, between 1.7–1.9 D). As can be seen in Fig. 11, changes in the orientation with respect to changing the halogen atom are nearly

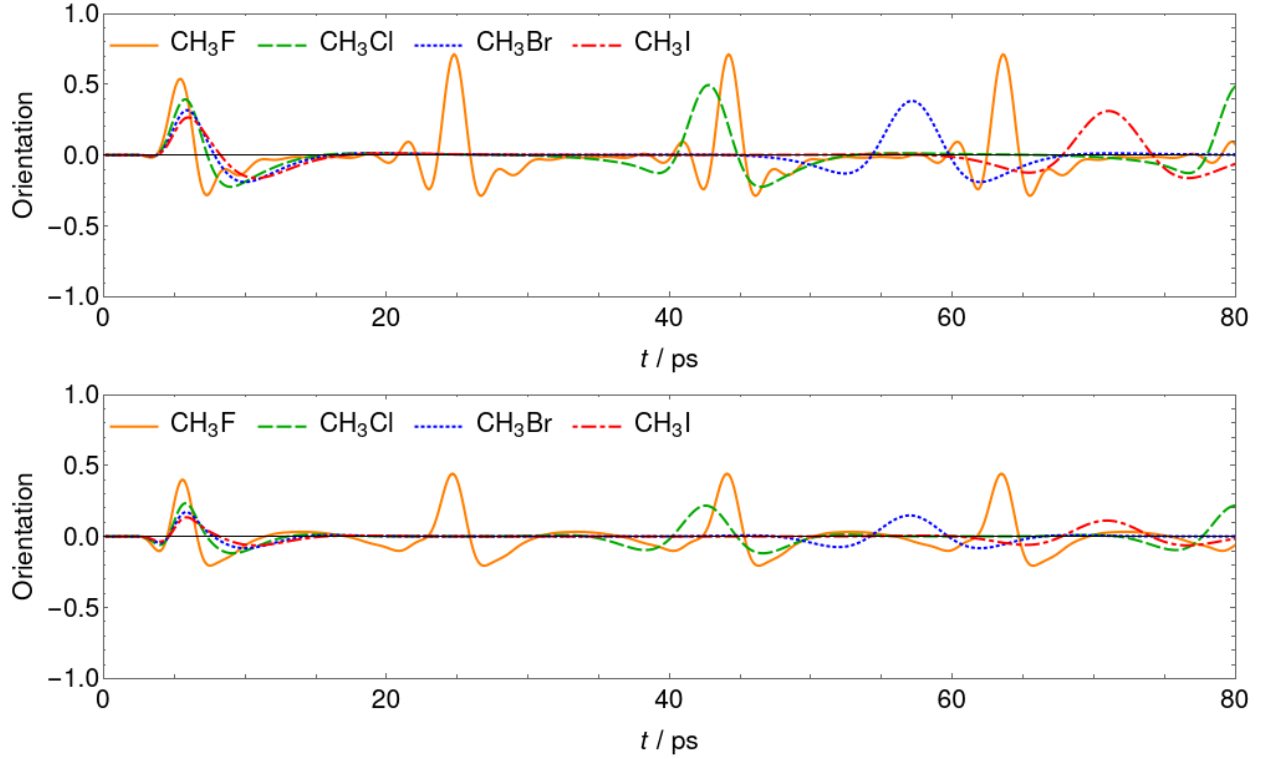


FIG. 11: Testing the effect of the molecular parameters in the alignment and orientation of the  $\text{CH}_3\text{X}$  molecules for a  $\nu/\text{THz} = 0.25$  (upper panel) and a  $0.333$  (lower panel) pulse. The polarizability was set to zero and the dipole moment was 2 D for all molecules. Pulse parameters:  $T/\text{K} = 5$ ,  $\text{FWHM}/\text{fs} = 2000$ , pulse position is 5 ps,  $I/\text{TW cm}^{-2} = 5 \times 10^{-4}$ ,  $\text{CEP} = \pi/2$ .

the same as in Figs. 8 and 9; therefore, it is understood that the rotational constants are responsible for the different molecular behavior. If the size of the halogen is increased, more rotational states will be populated at a given finite temperature, which decreases the maximal orientation. Furthermore, increasing the size of the halogen decreases the transition frequency between the rotational states, so the transition frequencies are further away from the central frequency of the pulse, which decreases the degree of excitation.

The computations summarized in Figs. 8 and 9 were repeated after setting the rotational constant to the  $\text{CH}_3\text{F}$  value for all molecules, resulting in nearly identical orientation for all the molecules. This confirms that the rotational constants determine the orientation in this situation, *i.e.*, when the molecules have similar permanent dipole moments.

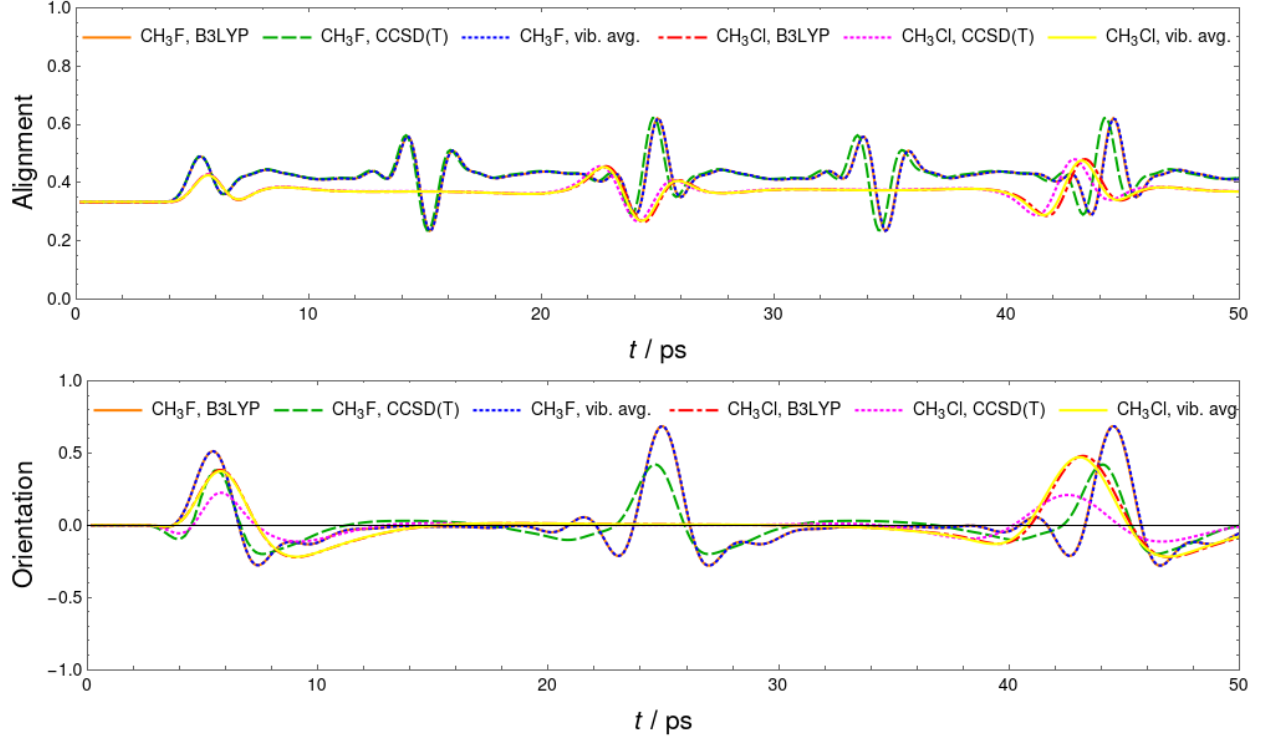


FIG. 12: Testing the effect of parameter accuracy on the alignment and orientation of  $\text{CH}_3\text{F}$  and  $\text{CH}_3\text{Cl}$ . The upper and lower panels show the alignment and orientation, respectively. The ‘B3LYP’ and ‘CCSD(T)’ curves correspond to using equilibrium molecular parameters obtained at the aug-cc-pV5Z B3LYP and aug-cc-pwCVQZ CCSD(T) levels (see Tables I and II), while the ‘vib. avg.’ curve (which accidentally coincides with the ‘B3LYP’ curve) was obtained using  $A_0$  and  $B_0$  rotational constants, and  $\mu_0$  dipole moment (see Table III). The pulse parameters chosen are as follows:  $T/\text{K} = 5$ ,  $\nu/\text{THz} = 0.25$ ,  $\text{FWHM}/\text{fs} = 2000$ , pulse position at 5 ps,  $I/\text{TW cm}^{-2} = 5 \times 10^{-4}$ , and  $\text{CEP} = \pi/2$ .

## 2. Sensitivity to the accuracy of molecular parameters

Figure 12 shows the A&O dynamics of  $\text{CH}_3\text{F}$  and  $\text{CH}_3\text{Cl}$ , obtained with parameters computed either at the highest, aug-cc-pwCVQZ CCSD(T) level or the much less expensive aug-cc-pV5Z B3LYP level, and also with using  $A_0$ ,  $B_0$ , and  $\mu_0$  instead of the equilibrium values. Similarly to the case of the optical pulse, the results obtained with the vibrationally averaged parameters and with the aug-cc-pV5Z B3LYP equilibrium parameters coincide.

One can observe from Fig. 12 that the revivals computed with the different parameter sets are not only drifting away with increasing time, but the maximal orientation is very different. This further emphasizes the need to use accurate rotational constants to obtain accurate orientation information.



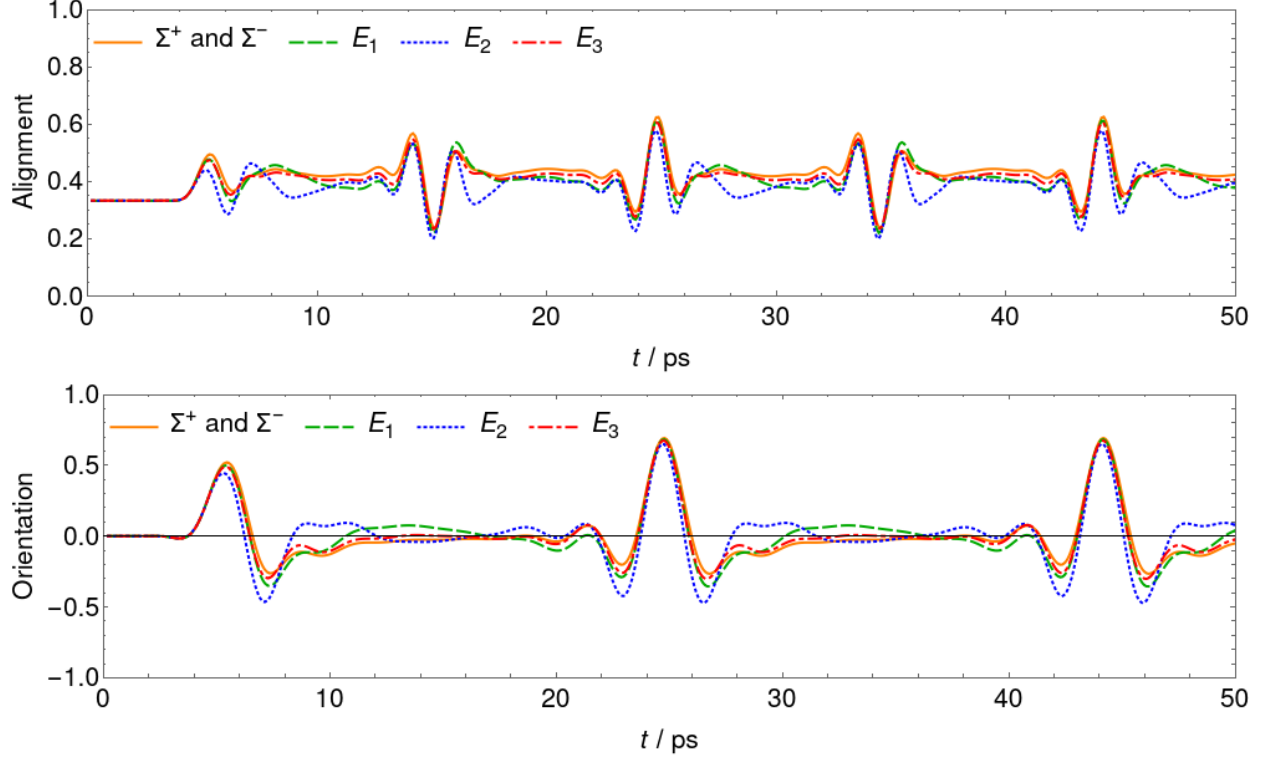


FIG. 13: Role of symmetry in the A&O dynamics of  $\text{CH}_3\text{F}$  (see text for details). Pulse parameters:  $T/\text{K} = 5$ ,  $\nu/\text{THz} = 0.25$ ,  $\text{FWHM}/\text{fs} = 2000$ , pulse position is 5 ps,  $I/\text{TW cm}^{-2} = 5 \times 10^{-4}$ , and  $\text{CEP} = \pi/2$ .

### 3. The role of symmetry and nuclear-spin-statistical weights

To complete the picture, we analyzed the role of symmetry for the THz pulse, as well. The dipole moment of  $\text{CH}_3\text{X}$  transforms as the  $\Sigma^-$  irrep of the  $D_\infty$  rotational group. This determines the dipole transition selection rules: the transition between states  $i$  and  $f$ , belonging to the  $\Gamma_i$  and  $\Gamma_f$  irreps, respectively, is allowed if  $\Sigma^+ \subseteq \Gamma_f \otimes \Sigma^- \otimes \Gamma_i$ , *i.e.*, the direct product contains the total symmetric irrep. Thus, the allowed transitions are the following:  $\Sigma^+ \leftrightarrow \Sigma^-$ ,  $E_1 \leftrightarrow E_1$ ,  $E_2 \leftrightarrow E_2$ , and  $E_3 \leftrightarrow E_3$ . In order to study how transitions with different symmetry contribute to the A&O dynamics of  $\text{CH}_3\text{F}$ , we made separate simulations for the subsets of irreps interconnected by the dipole interaction (see Fig. 13), where the NSSW of the given subset was 1, and all the others 0. These subsets are  $\{\Sigma^+, \Sigma^-\}$ ,  $\{E_1\}$ ,  $\{E_2\}$ ,  $\{E_3\}$ . The A&O curves are quite similar in each case, except for slight differences in the  $\{E_2\}$  curve towards the end of each revival. Contrary to the optical pulse scenario (see Fig. 5), no new revivals appear in Fig. 13 with respect to Fig. 8.

## VII. SUMMARY AND CONCLUSIONS

The laser-induced alignment and orientation (A&O) dynamics of the prolate symmetric-top  $\text{CH}_3\text{X}$  ( $\text{X} = \text{F}, \text{Cl}, \text{Br}$  and  $\text{I}$ ) molecules were investigated using standard quantum-chemistry software and the in-house LIMA0 [40] code. The molecular parameters required by LIMA0 for the A&O simulations, *i.e.*, the rotational constants, the dipole moment vectors, and the polarizability tensors, were computed using different levels of electronic-structure theory and employing a variety of basis sets. The numerical convergence of the molecular parameters toward the ultimate complete-basis-set full-configuration-interaction limit was investigated utilizing the focal-point-analysis (FPA) approach [59, 60]. The molecular parameters computed and employed in the LIMA0 simulations correspond to the equilibrium structure. Table III of this paper summarizes our most accurate estimates of these values. For  $\text{CH}_3\text{F}$  and  $\text{CH}_3\text{Cl}$ , vibrationally averaged rotational constants ( $A_0$  and  $B_0$ ) and dipoles ( $\mu_0$ ) were also determined and utilized in LIMA0 simulations.

The qualitative changes observed in the molecular parameters computed can be explained straightforwardly and these trends can be used to understand the effect of halogen substitution on the laser-induced A&O dynamics. The  $B_e$  rotational constant decreases in the  $\text{F} \rightarrow \text{Cl} \rightarrow \text{Br} \rightarrow \text{I}$  order, that is as the halogen gets heavier. Changes in  $A_e$  upon halogen substitution is much less pronounced and not monotonic. The dipole moments vary considerably less than the other molecular properties and it is a non-monotonous function of the atomic number of the halogen, having a maximum for  $\text{CH}_3\text{Cl}$ . Qualitatively, the dipole is determined by the partial charges on the carbon and halogen atoms, which depend on the electronegativity of these atoms, and the charge separation, which depends on the carbon-halogen bond length. These two properties show opposite trends with the increasing size of the halogen, and their effect on the dipole moment tend to cancel each other out. The polarizability anisotropy,  $\Delta\alpha$ , which determines the polarizability (field-induced dipole) interaction, increases with the size of the halogen:  $\Delta\alpha_{\text{CH}_3\text{F}} < \Delta\alpha_{\text{CH}_3\text{Cl}} < \Delta\alpha_{\text{CH}_3\text{Br}} < \Delta\alpha_{\text{CH}_3\text{I}}$ , with the largest difference found between  $\text{X} = \text{F}$  and  $\text{Cl}$ .

Sensitivity of the A&O results on the molecular parameters was tested extensively, showing that the A&O dynamics are most sensitive to the accuracy of the rotational constants, especially that of  $B$ . Interestingly, the A&O curves obtained using vibrationally averaged rotational constants and dipole moments are very similar to those resulting from the use

of the equilibrium values of these parameters computed at the inexpensive aug-cc-pV5Z B3LYP level. Using equilibrium molecular parameters obtained at the most sophisticated, aug-cc-pwCVQZ CCSD(T) level, results in slightly different A&O dynamics. This can be explained by the fact that, coincidentally,  $B_0$  and  $B_{e,a5Z\ B3LYP}$  happen to be very close to each other, while  $B_{e,awcQZ\ CCSD(T)}$  is a bit different from both of them. This relationship does not characterize the  $A$  rotational constants.

Our systematic computations demonstrate that a short and intense optical laser pulse, with a chosen wavelength of 800 nm, can be used to achieve non-adiabatic alignment, whereby the molecule interacts with the electric field through its polarizability. The time between the alternating alignment revivals (half revivals),  $T_{\text{rev}} = 1/(4cB_e)$ , is inversely proportional to the rotational constant; therefore, it increases with the size of the halogen. The maximal alignment is much smaller for  $\text{CH}_3\text{F}$  than for the other molecules. The maximal alignment for  $\text{CH}_3\text{F}$  depends linearly on the pulse intensity, at least in the interval studied, while the other three molecules show a saturation-type behavior. The maximal alignment decreases if the rotational constant is decreased, but increases with increased polarizability anisotropy. For the  $\text{CH}_3\text{X}$  molecules, the latter effect dominates, especially at large pulse intensities, resulting in much greater alignment for  $\text{CH}_3\text{Cl}$ ,  $\text{CH}_3\text{Br}$ , and  $\text{CH}_3\text{I}$  than for  $\text{CH}_3\text{F}$ . This behavior reflects the polarizability anisotropy of the four molecules. The contribution of the rotational states with different symmetry, weighed by their nuclear spin statistical weights (NSSW), was determined, demonstrating that certain alignment revivals cancel each other out in the averaged signal. Increasing the temperature decreases the maximal alignment, as expected.

Short and intense THz laser pulses can cause non-adiabatic orientation (and alignment) in the sample, with the time between the orientation revivals being twice as long as for the alignment. The field-dipole interaction is the dominant one in the case of THz pulses, and the interaction due to the polarizability of the systems can be neglected. The frequency of the THz pulses is in the range of the rotational transitions; however, for few-cycle pulses the central frequency does not have to be resonant with a specific transition for achieving A&O. Due to the short duration of the pulse, the bandwidth covers several rotational transitions. We investigated the orientation of the  $\text{CH}_3\text{X}$  molecules induced by experimentally feasible, intense few-cycle THz pulses with  $\nu = 0.25$  THz (equivalent to  $8.3\text{ cm}^{-1}$ ) and  $0.333$  THz (equivalent to  $11.1\text{ cm}^{-1}$ ) frequency and having a full width at half maximum of 2 picosec-

onds. For these pulses, the maximal orientation decreases with the size of the halogen; thus, contrary to the case of the optical pulse,  $\text{CH}_3\text{F}$  has the largest maximal A&O among the four molecules. The rotational constants determine the time between the revivals, similar to the optical-pulse case, but it is again the rotational constant which mainly determines the maximal orientation, as the  $\text{CH}_3\text{X}$  molecules have similar dipole moments. If the rotational constants are decreased, i.e., the size of the halogen is increased, more states will be populated at a given finite temperature, which lowers the maximal orientation. The transition frequency of the rotational transitions also decreases with decreasing rotational constants, leading to a smaller overlap between the bandwidth of the laser pulse and the rotational transitions (note that the rotational transitions of the  $\text{CH}_3\text{X}$  molecules relevant in the A&O dynamics simulations of this study are mostly smaller than the THz photon energies). In the case of  $\text{CH}_3\text{F}$ , we also studied the (nearly) adiabatic regime of the THz-pulse-induced A&O, showing much lower A&O than in the non-adiabatic case. A detailed investigation of the relation between the laser-induced rotational populations and the resulting A&O dynamics is planned in a future work.

## VIII. ACKNOWLEDGEMENTS

This research was supported by the János Bolyai Research Scholarship of the Hungarian Academy of Sciences, awarded to TSz, and by the ÚNKP-20-5 and ÚNKP-20-3 New National Excellence Program of the Ministry for Innovation and Technology from the source of the National Research, Development and Innovation Fund, awarded to TSz and IS, respectively. The Hungarian co-authors are also grateful to NKFIH for additional support (Grants No. FK134291, K119658, and K138233). ELI-ALPS is supported by the European Union and co-financed by the European Regional Development Fund (GI-NOP-2.3.6-15-2015-00001). KC and MUK acknowledge Project no. 2019-2.1.13-TÉT-IN-2020-00059 which has been implemented with the support provided from the National Research, Development and Innovation Fund of Hungary, financed under the 2019-2.1.13-TÉT-IN funding scheme.

## IX. DATA AVAILABILITY

The data that support the findings of this study are available from the corresponding author upon reasonable request.

## X. CONFLICT OF INTEREST

The authors have no conflicts to disclose.

- 
- [1] H. Stapelfeldt, T. Seideman, Colloquium: Aligning molecules with strong laser pulses, *Rev. Mod. Phys.* 75 (2003) 543–557.
  - [2] Y. Ohshima, H. Hasegawa, Coherent rotational excitation by intense nonresonant laser fields, *Int. Rev. Phys. Chem.* 29 (2010) 619–663.
  - [3] M. Lemeshko, R. V. Krems, J. M. Doyle, S. Kais, Manipulation of molecules with electromagnetic fields, *Mol. Phys.* 111 (2013) 1648–1682.
  - [4] C. P. Koch, M. Lemeshko, D. Sugny, Quantum control of molecular rotation, *Rev. Mod. Phys.* 91 (2019) 035005.
  - [5] M. Härtelt, B. Friedrich, Directional states of symmetric-top molecules produced by combined static and radiative electric fields, *J. Chem. Phys.* 128 (2008) 224313.
  - [6] A. Korobenko, V. Milner, Adiabatic field-free alignment of asymmetric top molecules with an optical centrifuge, *Phys. Rev. Lett.* 116 (2016) 183001.
  - [7] J. J. Larsen, H. Sakai, C. P. Safvan, I. Wendt-Larsen, H. Stapelfeldt, Aligning molecules with intense nonresonant laser fields, *J. Chem. Phys.* 111 (1999) 7774–7781.
  - [8] B. Friedrich, D. Herschbach, Alignment and trapping of molecules in intense laser fields, *Phys. Rev. Lett.* 74 (1995) 4623–4626.
  - [9] C. Z. Bisgaard, M. D. Poulsen, E. Péronne, S. S. Viftrup, H. Stapelfeldt, Observation of enhanced field-free molecular alignment by two laser pulses, *Phys. Rev. Lett.* 92 (2004) 173004.
  - [10] R. Damari, S. Kallush, S. Fleischer, Rotational control of asymmetric molecules: Dipole-versus polarizability-driven rotational dynamics, *Phys. Rev. Lett.* 117 (2016) 103001.

- [11] K. Sonoda, A. Iwasaki, K. Yamanouchi, H. Hasegawa, Field-free molecular orientation of nonadiabatically aligned OCS, *Chem. Phys. Lett.* 693 (2018) 114–120.
- [12] F. Rosca-Pruna, M. Vrakking, Experimental Observation of Revival Structures in Picosecond Laser-Induced Alignment of  $I_2$ , *Phys. Rev. Lett.* 87 (2001) 153902.
- [13] T. Seideman, Revival structure of aligned rotational wave packets, *Phys. Rev. Lett.* 83 (1999) 4971–4974.
- [14] B. Shepperson, A. S. Chatterley, A. A. Søndergaard, L. Christiansen, M. Lemesko, H. Stapelfeldt, Strongly aligned molecules inside helium droplets in the near-adiabatic regime, *J. Chem. Phys.* 147 (2017) 013946.
- [15] J. D. Pickering, B. Shepperson, L. Christiansen, H. Stapelfeldt, Alignment of the  $CS_2$  dimer embedded in helium droplets induced by a circularly polarized laser pulse, *Phys. Rev. A* 99 (2019) 043403.
- [16] K. F. Lee, D. M. Villeneuve, P. B. Corkum, A. Stolow, J. G. Underwood, Field-free three-dimensional alignment of polyatomic molecules, *Phys. Rev. Lett.* 97 (2006) 173001.
- [17] M. Artamonov, T. Seideman, Three-dimensional laser alignment of polyatomic molecular ensembles, *Mol. Phys.* 110 (2012) 885–896.
- [18] X. Ren, V. Makhija, V. Kumarappan, Multipulse three-dimensional alignment of asymmetric top molecules, *Phys. Rev. Lett.* 112 (2014) 173602.
- [19] J. J. Larsen, K. Hald, N. Bjerre, H. Stapelfeldt, T. Seideman, Three dimensional alignment of molecules using elliptically polarized laser fields, *Phys. Rev. Lett.* 85 (2000) 2470–2473.
- [20] I. Tutunnikov, L. Xu, R. W. Field, K. A. Nelson, Y. Prior, I. S. Averbukh, Enantioselective orientation of chiral molecules induced by terahertz pulses with twisted polarization, *Phys. Rev. Res.* 3 (2021) 013249.
- [21] S. Fleischer, Y. Zhou, R. W. Field, K. A. Nelson, Molecular orientation and alignment by intense single-cycle THz pulses, *Phys. Rev. Lett.* 107 (2011) 163603.
- [22] P. M. Felker, Rotational coherence spectroscopy: studies of the geometries of large gas-phase species by picosecond time-domain methods, *J. Phys. Chem.* 96 (1992) 7844–7857.
- [23] C. Schröter, J. C. Lee, T. Schultz, Mass-correlated rotational raman spectra with high resolution, broad bandwidth, and absolute frequency accuracy, *Proc. Natl. Acad. Sci.* 115 (2018) 5072–5076,.

- [24] C. Riehn, High-resolution pump–probe rotational coherence spectroscopy – rotational constants and structure of ground and electronically excited states of large molecular systems, *Chem. Phys.* 283 (2002) 297–329.
- [25] A. S. Chatterley, L. Christiansen, C. A. Schouder, A. V. Jørgensen, B. Shepperson, I. N. Cherepanov, G. Bighin, R. E. Zillich, M. Lemesko, H. Stapelfeldt, Rotational coherence spectroscopy of molecules in helium nanodroplets: Reconciling the time and the frequency domains, *Phys. Rev. Lett.* 125 (2020) 013001.
- [26] M. Nisoli, P. Decleva, F. Calegari, A. Palacios, F. Martín, Attosecond electron dynamics in molecules, *Chem. Rev.* 117 (2017) 10760–10825.
- [27] F. Krausz, M. Ivanov, Attosecond physics, *Rev. Mod. Phys.* 81 (2009) 163–234.
- [28] S. Kühn, M. Dumergue, S. Kahaly, S. Mondal, M. Füle, T. Csizmadia, B. Farkas, B. Major, Z. Várallyay, E. Cormier, M. Kalashnikov, F. Calegari, M. Devetta, F. Frassetto, E. Månsson, L. Poletto, S. Stagira, C. Vozzi, M. Nisoli, P. Rudawski, S. Maclot, F. Campi, H. Wikmark, C. L. Arnold, C. M. Heyl, P. Johnsson, A. L’Huillier, R. Lopez-Martens, S. Haessler, M. Boccum, F. Boehle, A. Vernier, G. Iaquaniello, E. Skantzakis, N. Papadakis, C. Kalpouzos, P. Tzallas, F. Lépine, D. Charalambidis, K. Varjú, K. Osvay, G. Sansone, The ELI-ALPS facility: the next generation of attosecond sources, *J. Phys. B* 50 (2017) 132002.
- [29] P. M. Kraus, B. Mignolet, D. Baykusheva, A. Rupenyan, L. Horný, E. F. Penka, G. Grassi, O. I. Tolstikhin, J. Schneider, F. Jensen, L. B. Madsen, A. D. Bandrauk, F. Remacle, H. J. Wörner, Measurement and laser control of attosecond charge migration in ionized iodoacetylene, *Science* 350 (2015) 790–795.
- [30] C. Z. Bisgaard, O. J. Clarkin, G. Wu, A. M. D. Lee, O. Gessner, C. C. Hayden, A. Stolow, Time-resolved molecular frame dynamics of fixed-in-space CS<sub>2</sub> molecules, *Science* 323 (2009) 1464–1468.
- [31] C. B. Madsen, L. B. Madsen, S. S. Viftrup, M. P. Johansson, T. B. Poulsen, L. Holmegaard, V. Kumarappan, K. A. Jørgensen, H. Stapelfeldt, Manipulating the torsion of molecules by strong laser pulses, *Phys. Rev. Lett.* 102 (2009) 073007.
- [32] E. Skantzakis, S. Chatziathanasiou, P. A. Carpeggiani, G. Sansone, A. Nayak, D. Gray, P. Tzallas, D. Charalambidis, E. Hertz, O. Faucher, Polarization shaping of high-order harmonics in laser-aligned molecules, *Sci. Rep.* 6 (2016) 39295.

- [33] O. Faucher, E. Prost, E. Hertz, F. Billard, B. Lavorel, A. A. Milner, V. A. Milner, J. Zyss, I. S. Averbukh, Rotational Doppler effect in harmonic generation from spinning molecules, *Phys. Rev. A* 94 (2016) 051402.
- [34] Y. Yang, L. Liu, J. Zhao, Y. Tu, J. Liu, Z. Zhao, Effect of ionization asymmetry on high harmonic generation from oriented CO in orthogonal two-color fields, *J. Phys. B-At. Mol. Opt.* 54 (2021) 144009.
- [35] E. Hamilton, T. Seideman, T. Ejdrup, M. D. Poulsen, C. Z. Bisgaard, S. S. Viftrup, H. Stapelfeldt, Alignment of symmetric top molecules by short laser pulses, *Phys. Rev. A* 72 (2005) 043402.
- [36] S. Luo, W. Hu, J. Yu, R. Zhu, L. He, X. Li, P. Ma, C. Wang, F. Liu, W. G. Roeterdink, S. Stolte, D. Ding, Rotational dynamics of quantum state-selected symmetric-top molecules in nonresonant femtosecond laser fields, *J. Phys. Chem. A* 121 (2017) 777–783.
- [37] S. Luo, S. Zhou, W. Hu, J. Yu, X. Li, P. Ma, L. He, C. Wang, F. Guo, Y. Yang, D. Ding, Identifying the multielectron effect on chemical bond rearrangement of CH<sub>3</sub>Cl molecules in strong laser fields, *J. Phys. Chem. A* 122 (2018) 8427–8432.
- [38] L. He, Y. Pan, Y. Yang, S. Luo, C. Lu, H. Zhao, D. Li, L. Song, S. Stolte, D. Ding, W. G. Roeterdink, Ion yields of laser aligned CH<sub>3</sub>I and CH<sub>3</sub>Br from multiple orbitals, *Chem. Phys. Lett.* 665 (2016) 141–146.
- [39] P. Sándor, A. Sissay, F. Mauger, M. W. Gordon, T. T. Gorman, T. D. Scarborough, M. B. Gaarde, K. Lopata, K. J. Schafer, R. R. Jones, Angle-dependent strong-field ionization of halomethanes, *J. Chem. Phys.* 151 (2019) 194308.
- [40] T. Szidarovszky, M. Jono, K. Yamanouchi, LIMA0: Cross-platform software for simulating laser-induced alignment and orientation dynamics of linear-, symmetric- and asymmetric tops, *Comp. Phys. Commun.* 228 (2018) 219–228.
- [41] T. Helgaker, P. Jørgensen, J. Olsen, *Molecular Electronic-Structure Theory*, Wiley, New York, 2000.
- [42] H. Hasegawa, Y. Ohshima, *Nonadiabatic Molecular Alignment and Orientation*, Springer International Publishing, Cham, 2015, pp. 45–64.
- [43] R. N. Zare, *Angular Momentum: Understanding Spatial Aspects in Chemistry and Physics*, Wiley, New York, 1988.



- [44] P. R. Bunker, P. Jensen, *Molecular Symmetry and Spectroscopy*, NRC Research Press, Ottawa, 2006.
- [45] <http://www.cfour.de>, CFOUR, a quantum chemical program package, last accessed on February 1, 2022.
- [46] <https://www.molpro.net/>, MOLPRO website, last accessed on February 1, 2022.
- [47] W. J. Hehre, L. Radom, P. v. R. Schleyer, J. A. Pople, *Ab Initio Molecular Orbital Theory*, Wiley-Interscience, New York, 1986.
- [48] F. Jensen, *Introduction to Computational Chemistry*, Wiley, Chichester, 2006.
- [49] C. C. J. Roothaan, New developments in molecular orbital theory, *Rev. Mod. Phys.* 23 (1951) 69–89.
- [50] C. Møller, M. S. Plesset, Note on an approximation treatment for many-electron systems, *Phys. Rev.* 46 (1934) 618–622.
- [51] R. Krishnan, M. J. Frisch, J. A. Pople, Contribution of triple substitutions to the electron correlation energy in fourth order perturbation theory, *J. Chem. Phys.* 72 (1980) 4244–4245.
- [52] J. Čížek, On the correlation problem in atomic and molecular systems. Calculation of wavefunction components in Ursell-type expansion using quantum-field theoretical methods, *J. Chem. Phys.* 45 (1966) 4256–4266.
- [53] G. D. Purvis, R. J. Bartlett, A full coupled-cluster singles and doubles model: The inclusion of disconnected triples, *J. Chem. Phys.* 76 (1982) 1910–1918.
- [54] K. Raghavachari, G. W. Trucks, J. A. Pople, M. Head-Gordon, A fifth-order perturbation comparison of electron correlation theories, *Chem. Phys. Lett.* 157 (1989) 479–483.
- [55] A. D. Becke, Density-functional exchange-energy approximation with correct asymptotic behavior, *Phys. Rev. A* 38 (1988) 3098–3100.
- [56] A. D. Becke, Density-functional thermochemistry. III. The role of exact exchange, *J. Chem. Phys.* 98 (1993) 5648–5652.
- [57] C. Lee, W. Yang, R. G. Parr, Development of the Colle–Salvetti correlation-energy formula into a functional of the electron density, *Phys. Rev. B* 37 (1988) 785–789.
- [58] T. H. Dunning Jr., Gaussian basis sets for use in correlated molecular calculations. I. The atoms boron through neon and hydrogen, *J. Chem. Phys.* 90 (1989) 1007–1023.
- [59] W. D. Allen, A. L. L. East, A. G. Császár, *Ab initio* anharmonic vibrational analyses of non-rigid molecules, in: J. Laane, M. Dakkouri, B. van der Veken, H. Oberhammer (Eds.),

- Structures and conformations of nonrigid molecules, Kluwer, Dordrecht, 1993, pp. 343–373.
- [60] A. G. Császár, W. D. Allen, H. F. Schaefer III, In pursuit of the *ab initio* limit for conformational energy prototypes, J. Chem. Phys. 108 (1998) 9751–9764.
- [61] M. Mantina, A. C. Chamberlin, R. Valero, C. J. Cramer, D. G. Truhlar, Consistent van der Waals radii for the whole main group, J. Phys. Chem. A 113 (2009) 5806–5812.
- [62] CRC Handbook of Chemistry and Physics, 84th Edition Edited by David R. Lide (National Institute of Standards and Technology), volume 126, 2004.
- [63] P. Schwerdtfeger, J. K. Nagle, 2018 table of static dipole polarizabilities of the neutral elements in the periodic table, Mol. Phys. 117 (2019) 1200–1225.
- [64] J. Demaison, J. Breidung, W. Thiel, D. Papousek, The equilibrium structure of methyl fluoride, Struct. Chem. 10 (1999) 129–133.
- [65] P. Jensen, S. Brodersen, G. Guelachvili, Determination of  $A_0$  for  $\text{CH}_3^{35}\text{Cl}$  and  $\text{CH}_3^{37}\text{Cl}$  from the  $\nu_4$  infrared and Raman bands, J. Mol. Spectrosc. 88 (1981) 378–393.
- [66] G. Graner, The methyl bromide molecule: A critical consideration of perturbations in spectra, J. Mol. Spectrosc. 90 (1981) 394–438.
- [67] H. Matsuura, J. Overend, Equilibrium structure of methyl iodide, J. Chem. Phys. 56 (1972) 5725–5727.
- [68] D. Papousek, Y. Hsu, H. Chen, P. Pracna, S. Klee, M. Winnemisser, Far Infrared Spectrum and Ground State Parameters of  $^{12}\text{CH}_3\text{F}$ , Journal of Molecular Spectroscopy 159 (1993) 33–41.
- [69] R. D. Nelson Jr., D. R. Lide, A. A. Maryott, Selected values of electric dipole moments for molecules in the gas phase, U.S. Dept. of Commerce, National Bureau of Standards, Washington, 1967.
- [70] R. D. Cowan, D. C. Griffin, Approximate relativistic corrections to atomic radial wave functions 66 (1976) 1010–1014.
- [71] K. Balasubramanian, Relativistic Effects in Chemistry, Wiley, New York, 1997.
- [72] G. Tarczay, A. G. Császár, W. Klopper, H. M. Quiney, Anatomy of relativistic energy corrections in light molecular systems, Mol. Phys. 99 (2001) 1769–1794.
- [73] G. Herzberg, Molecular Spectra and Molecular Structure: Electronic Spectra and Electronic Structure of Polyatomic Molecules, D. van Nostrand, New York, 1966.

- [74] A. K. Kandalam, B. Kiran, P. Jena, S. Pietsch, G. Ganteför, Superhalogens beget superhalogens: a case study of  $(\text{BO}_2)_n$  oligomers, *Phys. Chem. Chem. Phys.* 17 (2015) 26589–26593.
- [75] H. Pritchard, H. Skinner, The concept of electronegativity, *Chem. Rev.* 55 (1955) 745–786.
- [76] P. R. Bevington, D. K. Robinson, *Data Reduction and Error Analysis for the Physical Sciences*, Third Edition, McGraw-Hill, New York, 2003.
- [77] P. Szabó, S. Góger, J. Charry, M. R. Karimpour, D. V. Fedorov, A. Tkatchenko, Four-dimensional scaling of dipole polarizability in quantum systems. [arXiv:2010.11809](https://arxiv.org/abs/2010.11809).
- [78] T. Brabec, F. Krausz, Intense few-cycle laser fields: Frontiers of nonlinear optics, *Rev. Mod. Phys.* 72 (2000) 545–591.